The method of images in thermoelasticity with an application to wafer heating

Daniel W. M. Veldman, Rob H. B. Fey, Hans Zwart, Marc M. J. van de Wal, Joris D. B. J. van den Boom & Henk Nijmeijer

Published online: 07 Jul 2021.

Submit your article to this journal ↗

Article views: 73

View related articles ↗

View Crossmark data ↗

Taylor & Francis
Taylor & Francis Group

The method of images in thermoelasticity with an application to wafer heating

Daniel W. M. Veldman[a] (iD), Rob H. B. Fey[a] (iD), Hans Zwart[a,b] (iD), Marc M. J. van de Wal[c], Joris D. B. J. van den Boom[d], and Henk Nijmeijer[a] (iD)

[a]Department of Mechanical Engineering, Eindhoven University of Technology, Eindhoven, the Netherlands; [b]Department of Applied Mathematics, University of Twente, Enschede, the Netherlands; [c]ASML Research, ASML, Veldhoven, the Netherlands; [d]ASML D&E Machine Conditioning, ASML, Veldhoven, the Netherlands

ABSTRACT

The well-known method of images relates the solution of the heat equation on $\mathbb{R}^n$ (typically $n = 2$ or $n = 3$) to the solution of the heat equation on certain spatial subdomains Ω of $\mathbb{R}^n$. By reformulating the method of images in terms of a convolution kernel, two novel extensions are obtained in this paper. First, the method of images is extended from thermal problems to thermoelastic problems, that is, it is demonstrated how the heat-induced deformations on $\mathbb{R}^n$ can be related to the heat-induced deformations on certain subdomains Ω of $\mathbb{R}^n$. Secondly, an explicit expression for the convolution kernel for the disk is obtained. This enables the application of the method of images to circular domains to which it could not be applied before. The two obtained extensions lead to a computationally efficient simulation method for repetitive heat loads on a disk. In a representative simulation example of wafer heating, the proposed method is more than ten times faster than a conventional Finite Element approach.

1. Introduction

The Method of Images (MoI) relates the solution of the heat equation with constant coefficients on $\mathbb{R}^n$, typically $n = 2$ or $n = 3$, to solutions of the heat equation on certain subdomains $\Omega \subset \mathbb{R}^n$. Analytic expressions for the solution on $\mathbb{R}^n$ can be obtained using the fundamental solution of the heat equation, see for example [1, 2]. The MoI is therefore typically used to derive analytic and semi-analytic expressions for the solution of heat conduction problems on bounded domains, see for example [3–5]. In most cases, the method is applied for zero Neumann boundary conditions (BCs), but the method has been extended to a variety of other BCs such as (zero) Dirichlet or Robin BCs, see [1, 6, 7]. In most cases, the material properties are assumed to be constant, but extensions to multilayered materials in which the material properties are piecewise constant also exist [6, 7]. The MoI dates back at least to the nineteenth century, see [8], but might well be even older and has also applied to problems in elasticity, see for example [9, 10].

The MoI is not only of interest for the derivation of (semi)-analytical expressions for the temperature field on certain subdomains, but can also be used to reduce the computational cost for the simulation of heat conduction problems with repetitive sources [11]. For such processes, the

---

CONTACT Daniel W. M. Veldman ✉ d.w.m.veldman@gmail.com ◨ Eindhoven University of Technology, P.O. Box 513, 5600 MB Eindhoven, the Netherlands.
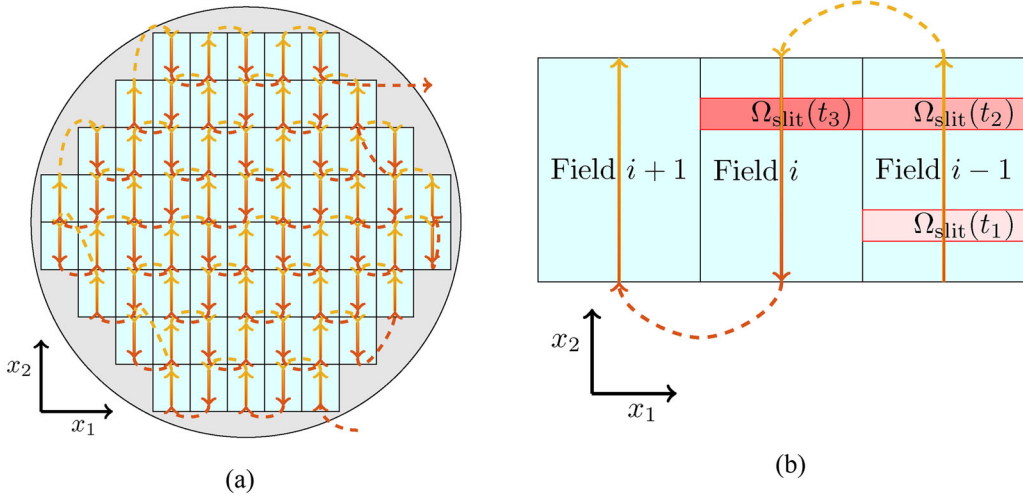
Figure 1. An example of a repetitive heat load that occurs in a lithography process (wafer heating). In this process, a pattern of electronic connections is projected onto the wafer in an area $\Omega_{\text{slit}}(t)$ called the slit that moves over the wafer surface. The light used to project the pattern results in a (uniform) heat load applied in $\Omega_{\text{slit}}(t)$. Because each field is scanned in the same way, the applied heat load is repetitive. (a) A typical expose pattern in lithography. The heat load scans multiple fields (light blue rectangles) on a silicon wafer (gray disk) which results in a meandering path (red and orange arrows). (b) A detailed view of the scanning of fields $i - 1$, i, and $i + 1$ (the three light blue rectangles). The heat load is applied in a rectangular area $\Omega_{\text{slit}}(t)$ which is displayed at three time instances $t_1 < t_2 < t_3$ (red rectangles).

temperature field on the unbounded domain $\mathbb{R}^n$ can be constructed effectively by exploiting the translation, rotation, and time invariance of the heat equation on $\mathbb{R}^n$. The MoI is then applied to obtain the solution on the subdomain $\Omega \subset \mathbb{R}^n$ of interest.

Repetitive heat loads occur in many industrial applications where a surface is treated by the (small) spot of a laser beam. In these applications, multiple passings of the laser over the surface occur. The heat load applied during each passing is the same up to a translation and/or rotation in space and a shift in time. Examples of such processes are the laser hardening of metals [12–14], additive manufacturing [15–17], and wafer heating [11, 18, 19]. In the latter application, a pattern of electronic connections is projected onto a silicon wafer, see Figure 1. The light used to project the pattern heats up the wafer which leads to thermal expansion and a degraded imaging quality. Note that the pattern is projected consecutively onto all fields (the light blue rectangles in Figure 1) and that the same pattern of electronic connections is projected in each field. It is therefore natural to consider the scanning of one field as one passing of the heat load. Fast and sufficiently accurate simulation of this process is needed to improve the imaging quality of the latest generation wafer scanners.

It should be noted that the assumption of constant material properties is problematic when temperature increases are large. However, semi-analytic models have also been developed for applications where the material properties are certainly not constant such as welding [4, 5] and additive manufacturing [17]. In contrast to these applications, the temperature increases encountered in wafer heating are small, that is, smaller than one Kelvin, and the material properties can assumed to be constant. This makes the MoI particularly suitable for the wafer heating application.

However, the wafer heating application comes with two specific difficulties. The first difficulty is that the spatial domain is a disk (see Figure 1) and that, to the best of our knowledge, the MoI has only been applied to box-shaped (also called orthogonal) domains. The second difficulty is that, rather than the temperature field, the heat-induced deformation is of interest because local deformation eventually determines the imaging quality of the lithographic process. To the best of our knowledge, the MoI has only been applied to the temperature field and not to the heat-induced deformations.

This paper addresses these two difficulties by reformulating the MoI in terms of a convolution kernel. Two novel extensions are obtained. First, it is shown how the MoI can be applied in thermo-elasticity, that is, it is shown how the heat-induced deformation in a subdomain $\Omega \subset \mathbb{R}^n$ can be computed based on the heat-induced deformation on $\mathbb{R}^n$. This extension is based on the displacement potential function, see for example [20–22], which means that in almost all cases an additional correction is needed to satisfy the mechanical BCs. Secondly, it is shown how the MoI can be applied to a disk. This extension is found by solving a certain Partial Differential Equation (PDE) for the convolution kernel. These two extensions enable the efficient simulation of thermomechanical systems on a disk-shaped spatial domains. A representative wafer heating simulation demonstrates that the developed methods can reduce the required computational time by more than a factor ten compared to a conventional Finite Element (FE) analysis on a similar grid and with a similar accuracy.

The remainder of this paper is organized as follows. In Section 2, the considered class of thermomechanical systems and their response to repetitive heat loads is introduced. In Section 3, the MoI for heat conduction problems is reformulated in terms of a convolution kernel and extended to thermoelastic problems. Section 4 contains several examples that demonstrate how the general theory from Section 3 can be applied to specific spatial domains $\Omega \subset \mathbb{R}^n$ including a disk. The efficiency of the MoI for the simulation of thermomechanical problems with repetitive heat sources is then demonstrated for a wafer heating application in Section 5. Finally, Section 6 contains the conclusions and recommendations.

2. Problem description

2.1. Notation

The following notation will be used. Scalars are denoted by italic letters, for example t, κ, and T_0 denote scalars. Vectors are denoted by bold lower-case Roman letters, for example $\mathbf{x}$ denotes a vector. Unless specified otherwise, vectors are column vectors. Matrices are denoted by bold capital Roman letters or bold Greek letters, for example $\mathbf{I}$ and $\boldsymbol{\sigma}$ denote matrices. The transpose of a vector or a matrix is indicated by $\top$. Components of vectors and matrices are again scalars and are thus denoted by lower-case italic letters, for example a vector $\mathbf{x} \in \mathbb{R}^n$ can be written as $\mathbf{x} = [x_1, x_2, ..., x_n]^\top$. The Euclidean inner product is denoted by $\mathbf{x} \cdot \mathbf{y} = x_1 y_1 + x_2 y_2 + ... + x_n y_n$ and the Euclidean norm is denoted by $\|\mathbf{x}\| := \sqrt{\mathbf{x} \cdot \mathbf{x}}$.

The same conventions are used with respect to functions, for example $T(\mathbf{x}, t), \mathbf{u}(\mathbf{x}, t),$ and $\boldsymbol{\sigma}(\mathbf{x}, t)$ denote scalar-valued, vector-valued, and matrix-valued functions depending on the vector $\mathbf{x}$ and the scalar variable t, respectively, and $u_1(\mathbf{x}, t)$ denotes the first component of $\mathbf{u}(\mathbf{x}, t)$. The derivative of a scalar-valued function $T(\mathbf{x}, t)$ w.r.t. $\mathbf{x}$ is a row vector $\partial T / \partial \mathbf{x} = [\partial T / \partial x_1, \partial T / \partial x_2, ..., \partial T / \partial x_n]$, whereas the gradient w.r.t. $\mathbf{x}$ is a column vector $\nabla T = [\partial T / \partial \mathbf{x}]^\top$. When $\mathbf{x}$ are Cartesian coordinates, the gradient w.r.t. $\mathbf{x}$ of an $\mathbb{R}^n$-valued function $\mathbf{u}(\mathbf{x}, t)$ is an $\mathbb{R}^{n \times n}$-valued function which has the gradients of its components as columns, that is $\nabla \mathbf{u} = [\nabla u_1, \nabla u_2, ... \nabla u_n]$. The divergence w.r.t. $\mathbf{x}$ of an $\mathbb{R}^n$-valued vector field $\mathbf{u}(\mathbf{x}, t)$ is a scalar-valued function $\nabla \cdot \mathbf{u} = \partial u_1 / \partial x_1 + \partial u_2 / \partial x_2 + ... + \partial u_n / \partial x_n$. The divergence of a $\mathbb{R}^{n \times n}$-valued function $\boldsymbol{\sigma}(\mathbf{x}, t)$ is a vector and is taken column-wise, that is $\nabla \cdot \boldsymbol{\sigma} = [\nabla \cdot \boldsymbol{\sigma}_1, \nabla \cdot \boldsymbol{\sigma}_2, ..., \nabla \cdot \boldsymbol{\sigma}_n]^\top$, where $\boldsymbol{\sigma}_i$ denotes the i-th column of $\boldsymbol{\sigma}$. The Laplacian of a scalar-valued function $T(\mathbf{x}, t)$ is a scalar-valued function $\nabla^2 T = \partial^2 T / \partial x_1^2 + \partial^2 T / \partial x_2^2 + ... + \partial^2 T / \partial x_n^2$. The Laplacian of an $\mathbb{R}^n$-valued function $\mathbf{u}(\mathbf{x}, t)$ is taken component-wise, that is $\nabla^2 \mathbf{u} = [\nabla^2 u_1, \nabla^2 u_2, ..., \nabla^2 u_n]^\top$. The Dirac delta is denoted by δ.

2.2. Linear quasi-static thermoelasticity

The equations of thermoelasticity considered in this paper are of the same form for three-dimensional (3-D) and two-dimensional (2-D) problems. The spatial domain $\Omega \subset \mathbb{R}^n$ can thus be 3-D

or 2-D, that is, $n = 3$ or $n = 2$. The spatial coordinates in a Cartesian coordinate system are denoted by $\mathbf{x} \in \Omega \subset \mathbb{R}^n$. The edge of Ω is denoted by $\partial\Omega$. Time is denoted by t and is considered during a time interval $I := [0, t_1]$. At the initial time $t = 0$, the solid has a constant temperature T_0 and is stress-free.

The equations of linear thermoelasticity for an isotropic solid with constant material properties take the form [21]

$$c\frac{\partial T_\Omega}{\partial t} = \kappa\nabla^2 T_\Omega - h_0 T_\Omega + Q_\Omega, \tag{1a}$$

$$\mu\nabla^2 \mathbf{u}_\Omega + (\mu + \lambda)\nabla(\nabla \cdot \mathbf{u}_\Omega) - k_0\mathbf{u}_\Omega = (2\mu + n\lambda)\alpha\nabla T_\Omega, \tag{1b}$$

where $Q_\Omega(\mathbf{x}, t) : \Omega \times I \to \mathbb{R}$ [W/m^n] is the applied heat load, $T_\Omega(\mathbf{x}, t) : \Omega \times I \to \mathbb{R}$ [K] denotes the temperature increase (relative to the reference temperature T_0), and $\mathbf{u}(\mathbf{x}, t) : \Omega \times I \to \mathbb{R}^n$ [m] denotes the displacement (relative to the stress-free reference configuration at $t = 0$). Furthermore, c [J/m^n/K] denotes the heat capacity (per unit of Ω), κ [W/m^{n-2}/K] is the thermal conductivity (per unit of $\partial\Omega$), μ and λ [N/m^{n-1}] are the Lamé parameters, and α [1/K] is the coefficient of thermal expansion. The Lamé parameter μ is also known as the shear modulus and λ is characterizes the (in)compressability. The parameters $h_0 \geq 0$ [W/m^n/K] and $k_0 \geq 0$ [N/m^{n+1}] are typically zero for 3-D problems, but can be used to account for certain external heat fluxes and forces in 2-D problems as will be demonstrated in Section 5. Note that inertia effects have been neglected in the force balance (1b), which is a common assumption in thermoelasticity, see for example [21, 22].

The parameters c, κ, μ, and λ in (1) are different in 3-D problems and in 2-D plane stress and plane strain problems. For 3-D problems

$$c = \rho c_m, \qquad \kappa = k, \qquad \mu = \frac{E}{2(1 + \nu)}, \tag{2a}$$

$$\lambda = \frac{\nu E}{(1 + \nu)(1 - 2\nu)}, \tag{2b}$$

where ρ [kg/m^3] denotes the mass density, c_m [J/kg/K] is the heat capacity per unit mass (or specific heat capacity), k [W/K/m] is the thermal conductivity, E [N/m^2] is the Young's modulus, and ν [$-$] is Poisson's ratio. For 2-D plane-stress problems used in the modeling of thin plates

$$c = \rho c_m H, \qquad \kappa = kH, \qquad \mu = \frac{EH}{2(1 + \nu)}, \tag{3a}$$

$$\lambda = \frac{\nu E H}{1 - \nu^2}, \tag{3b}$$

where H [m] denotes the thickness of the considered plate. For 2-D plane-strain problems used in the modeling of thick plates, (3b) is changed to

$$\lambda = \frac{\nu E H}{(1 + \nu)(1 - 2\nu)}, \tag{3c}$$

and the other parameters are the same as in (3a).

The PDEs (1) should be considered with BCs and initial conditions (ICs). Thermal BCs for (1a) are typically formulated in terms of the temperature $T_\Omega(\mathbf{x}, t)$ and the heat flux normal to the edge

$$q_{\Omega, n}(\mathbf{x}, t) = \mathbf{q}_\Omega(\mathbf{x}, t) \cdot \mathbf{n}(\mathbf{x}), \tag{4a}$$

where $\mathbf{n}(\mathbf{x}) \in \mathbb{R}^n$ denotes the outward pointing unit normal at the point $\mathbf{x} \in \partial\Omega$ and $\mathbf{q}_\Omega(\mathbf{x}, t) : \Omega \times I \to \mathbb{R}^n$ [W/m^{n-1}] denotes the heat flux

$$q_\Omega(\mathbf{x}, t) = \kappa \nabla T_\Omega(\mathbf{x}, t). \tag{4b}$$

Note that the first term on the Right Hand Side (RHS) of (1a) can be recognized as the divergence of the heat flux, that is as $\nabla \cdot \mathbf{q}_\Omega$. Mechanical BCs for (1b) are usually formulated in terms of $\mathbf{u}_\Omega(\mathbf{x}, t)$ and the traction forces

$$\mathbf{t}_{\Omega, n}(\mathbf{x}, t) = \boldsymbol{\sigma}_\Omega(\mathbf{x}, t)\mathbf{n}(\mathbf{x}), \tag{5a}$$

where $\mathbf{x} \in \partial\Omega$ and the stress $\boldsymbol{\sigma}_\Omega(\mathbf{x}, t) : \Omega \times I \to \mathbb{R}^{n \times n}$ [N/m^{n-1}] is given by the constitutive relation [21, 22]

$$\boldsymbol{\sigma}_\Omega = \mu\left(\nabla\mathbf{u}_\Omega + (\nabla\mathbf{u}_\Omega)^\top\right) + \mathbf{I}(\lambda\nabla \cdot \mathbf{u}_\Omega - (2\mu + n\lambda)\alpha T_\Omega), \tag{5b}$$

where $\mathbf{I}$ denotes the $n \times n$ identity matrix. Note that the force balance (1b) can be written as $\nabla \cdot \boldsymbol{\sigma} - k_0\mathbf{u}_\Omega = \mathbf{0}$. In view of the wafer heating application that will be presented in Section 5, this paper mainly focuses on the perfectly insulated and traction force free BCs

$$q_{\Omega, n} = 0, \text{ on } \partial\Omega \times I, \tag{6a}$$

$$\mathbf{t}_{\Omega, n} = \mathbf{0}, \text{ on } \partial\Omega \times I, \tag{6b}$$

but modifications of the proposed approach to accommodate other BCs will be indicated as well. As it is assumed that the solid has a constant temperature T_0 and is stress free at $t = 0$, all ICs are zero.

Remark 1. When $k_0 > 0$, the solution $\mathbf{u}_\Omega(\mathbf{x}, t)$ of (1b) is unique for any choice of mechanical BCs. When $k_0 = 0$, the solution $\mathbf{u}_\Omega(\mathbf{x}, t)$ of (1b) with BCs (6b) is unique up to $(n + 1)n/2$ rigid body modes, see for example [23]. The solution $\mathbf{u}_\Omega(\mathbf{x}, t)$ should then be made unique by imposing $(n + 1)n/2$ additional conditions on $\mathbf{u}_\Omega(\mathbf{x}, t)$.

2.3. The displacement potential

The displacement field $\mathbf{u}_\Omega(\mathbf{x}, t) : \Omega \times I \to \mathbb{R}^n$ resulting from a temperature field $T_\Omega(\mathbf{x}, t) : \Omega \times I \to \mathbb{R}$ can be obtained using the displacement potential $\psi_\Omega(\mathbf{x}, t) : \Omega \times I \to \mathbb{R}$, see for example [20–22]. In this method, the displacement field $\mathbf{u}_\Omega(\mathbf{x}, t)$ is decomposed into two parts

$$\mathbf{u}_\Omega(\mathbf{x}, t) = \mathbf{u}_\Omega^{(T)}(\mathbf{x}, t) + \mathbf{u}_\Omega^{(BC)}(\mathbf{x}, t), \tag{7a}$$

where $\mathbf{u}_\Omega^{(T)}(\mathbf{x}, t)$ is equal to the gradient of the displacement potential $\psi_\Omega(\mathbf{x}, t)$, that is

$$\mathbf{u}_\Omega^{(T)}(\mathbf{x}, t) = \nabla\psi_\Omega(\mathbf{x}, t). \tag{7b}$$

Substituting (7b) into (1b) yields

$$\mu\nabla^2\nabla\psi_\Omega + (\mu + \lambda)\nabla\nabla^2\psi_\Omega - k_0\nabla\psi_\Omega = (2\mu + n\lambda)\alpha\nabla T_\Omega, \tag{8}$$

where it was used that $\nabla \cdot \nabla = \nabla^2$ by definition. Using that $\nabla^2\nabla = \nabla\nabla^2$, this equation can be rewritten as

$$(2\mu + \lambda)\nabla\nabla^2\psi_\Omega - k_0\nabla\psi_\Omega = (2\mu + n\lambda)\alpha\nabla T_\Omega. \tag{9}$$

This equation is satisfied if $\psi_\Omega(\mathbf{x}, t)$ satisfies

$$(2\mu + \lambda)\nabla^2\psi_\Omega - k_0\psi_\Omega = (2\mu + n\lambda)\alpha T_\Omega. \tag{10}$$

Any solution $\psi_\Omega(\mathbf{x}, t)$ of (10) thus corresponds to a particular solution $\mathbf{u}_\Omega^{(T)}(\mathbf{x}, t)$ of (1b) through (7b).

Note that (10) is a second-order PDE for $\psi_\Omega(\mathbf{x}, t)$, which means that one BC can be specified for $\psi_\Omega(\mathbf{x}, t)$. However, there are n mechanical BCs needed to define a unique displacement field

$\mathbf{u}_\Omega(\mathbf{x}, t)$, see for example (6b). There is thus not sufficient freedom in the BCs for $\psi_\Omega(\mathbf{x}, t)$ in (10) to ensure that the corresponding displacement field $\mathbf{u}_\Omega^{(T)}(\mathbf{x}, t)$ will satisfy the mechanical BCs. An additional correction $\mathbf{u}_\Omega^{(BC)}(\mathbf{x}, t)$ is used to assure that the displacement field $\mathbf{u}_\Omega(\mathbf{x}, t)$ in (7a) does satisfy the desired mechanical BCs. Because $\mathbf{u}_\Omega^{(T)}(\mathbf{x}, t)$ has been constructed to satisfy (1b), $\mathbf{u}_\Omega^{(BC)}(\mathbf{x}, t)$ should satisfy

$$\mu \nabla^2 \mathbf{u}_\Omega^{(BC)} + (\mu + \lambda)\nabla\left(\nabla \cdot \mathbf{u}_\Omega^{(BC)}\right) - k_0 \mathbf{u}_\Omega^{(BC)} = \mathbf{0}, \tag{11}$$

The BCs for $\mathbf{u}_\Omega^{(BC)}(\mathbf{x}, t)$ follow by substituting (7a) into the desired mechanical BCs for $\mathbf{u}_\Omega(\mathbf{x}, t)$. For the BCs (6b), this for example leads to

$$\boldsymbol{\sigma}_\Omega^{(BC)}(\mathbf{x}, t)\mathbf{n}(\mathbf{x}) = -\boldsymbol{\sigma}_\Omega^{(T)}(\mathbf{x}, t)\mathbf{n}(\mathbf{x}), \tag{12}$$

where $\boldsymbol{\sigma}^{(T)}(\mathbf{x}, t)$ denotes the stress obtained by setting $\mathbf{u}_\Omega(\mathbf{x}, t) \equiv \mathbf{u}_\Omega^{(T)}(\mathbf{x}, t)$ in (5b) and

$$\boldsymbol{\sigma}^{(BC)} = \mu\left(\nabla \mathbf{u}_\Omega^{(BC)} + \left(\nabla \mathbf{u}_\Omega^{(BC)}\right)^\top\right) + \lambda \mathbf{I} \nabla \cdot \mathbf{u}_\Omega^{(BC)}. \tag{13}$$

Remark 2. It is not clear how the BC for (10) should be chosen. Possible choices are for example the Dirichlet BC $\psi_\Omega(\mathbf{x}, t) = 0$ or the Neumann BC $\nabla \psi_\Omega(\mathbf{x}, t) \cdot \mathbf{n}(\mathbf{x}) = 0$. As different choices for the BC will lead to different solutions $\psi_\Omega(\mathbf{x}, t)$, the decomposition (7a) is also not unique. The BC for (10) will be further addressed in Section 3.

Note that when $\Omega = \mathbb{R}^n$ and $k_0 > 0$, the only solution of (11) is $\mathbf{u}_{\mathbb{R}^n}^{(BC)}(\mathbf{x}, t) \equiv \mathbf{0}$ (under the natural assumption that $\boldsymbol{\sigma}_{\mathbb{R}^n}^{(BC)}(\mathbf{x}, t) \to \mathbf{0}$ for $\|\mathbf{x}\| \to \infty$), see for example [23]. The decomposition (7a) then thus reduces to

$$\mathbf{u}_{\mathbb{R}^n}(\mathbf{x}, t) = \mathbf{u}_{\mathbb{R}^n}^{(T)}(\mathbf{x}, t) = \nabla \psi_{\mathbb{R}^n}(\mathbf{x}, t), \tag{14}$$

where it should be noted that the solution $\psi_{\mathbb{R}^n}(\mathbf{x}, t)$ of (10) is also unique when $k_0 > 0$, see for example [2]. When $k_0 = 0$, (14) still holds. This follows because the only solutions $\mathbf{u}_{\mathbb{R}^n}^{(BC)}(\mathbf{x}, t)$ of (11) (again assuming that $\boldsymbol{\sigma}_{\mathbb{R}^n}^{(BC)}(\mathbf{x}, t) \to \mathbf{0}$ for $\|\mathbf{x}\| \to \infty$) are linear combinations of the $(n + 1)n/2$ rigid body modes, which can also be included in $\mathbf{u}^{(T)}(\mathbf{x}, t)$. To see that this is the case, note that a displacement potential of the form

$$\psi_{\mathbb{R}^n, 0}(\mathbf{x}) = \sum_{i=1}^n c_i x_i + \sum_{\substack{i,j=1 \\ i \neq j}}^n c_{ij} x_i x_j, \tag{15}$$

where $c_i, c_{i,j} \in \mathbb{R}$ are constants, satisfies $\nabla^2 \psi_{\mathbb{R}^n, 0}(\mathbf{x}, t) \equiv 0$. It is thus always possible to add a solution of the form (15) to a solution $\psi_{\mathbb{R}^n}(\mathbf{x}, t)$ of (10) when $k_0 = 0$. Note that computing $\mathbf{u}_{\mathbb{R}^n, 0}^{(T)} = \nabla \psi_{\mathbb{R}^n, 0}$ shows that the constants c_i represent n translations and the coefficients c_{ij} represent $(n-1)n/2$ (linearized) rotations. The $n + (n-1)n/2 = (n+1)n/2$ rigid body modes can thus be obtained through a displacement potential of the form (15).

2.4. Repetitive heat sources

In many manufacturing processes such as the wafer heating problem in Figure 1, the applied heat load Q_Ω consists of multiple similar passings (in the wafer heating problem, one passing is the scanning of one field). The only difference between two passings is a translation and/or rotation in space and a shift in time. Such translations and rotations are more conveniently described on $\mathbb{R}^n$ and not on a subdomain $\Omega \subset \mathbb{R}^n$. It is therefore useful to define the extension $Q_{\Omega, \infty}(\mathbf{x}, t) : \mathbb{R}^n \times I \to \mathbb{R}$ of a heat load $Q_\Omega(\mathbf{x}, t) : \Omega \times I \to \mathbb{R}$ as
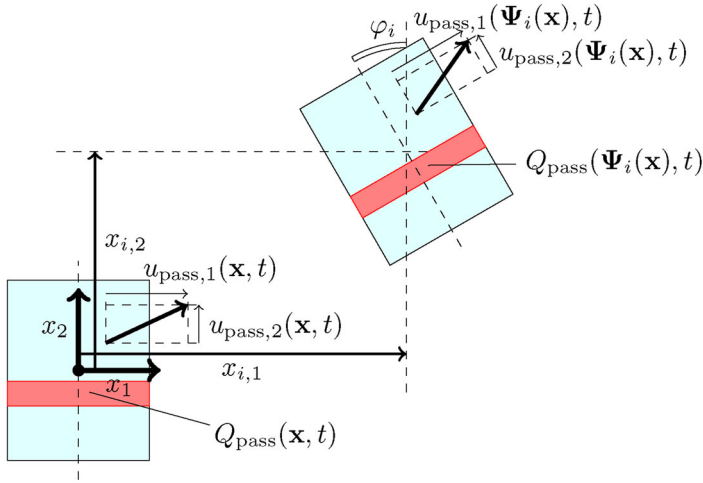
Figure 2. The mapping $\Psi_i(\mathbf{x})$ represents a translation along $\mathbf{x}_i = [x_{i,1}, y_{i,2}]^\top$ followed by a rotation over φ_i.

$$Q_{\Omega,\infty}(\mathbf{x}, t) = \begin{cases} Q_\Omega(\mathbf{x}, t) & \text{for } \mathbf{x} \in \Omega, \\ 0 & \text{otherwise.} \end{cases} \quad (16)$$

The temperature and the displacement fields that satisfy (1) with $Q_\Omega(\mathbf{x}, t) = Q_{\Omega,\infty}(\mathbf{x}, t)$ are denoted by $T_{\Omega,\infty}(\mathbf{x}, t) : \mathbb{R}^n \times I \to \mathbb{R}$ and $\mathbf{u}_{\Omega,\infty}(\mathbf{x}, t) : \mathbb{R}^n \times I \to \mathbb{R}^n$, respectively.

In this paper, a heat load $Q_\Omega(\mathbf{x}, t)$ is called repetitive if its extension $Q_{\Omega,\infty}(\mathbf{x}, t)$ to $\mathbb{R}^2$ as in (16) can be written as

$$Q_{\Omega,\infty}(\mathbf{x}, t) = \sum_{i=1}^N Q_{\text{pass}}(\Psi_i(\mathbf{x}), t - \tau_i), \quad (17)$$

where $Q_{\text{pass}}(\mathbf{x}, t) : \mathbb{R}^n \times I \to \mathbb{R}$ represents the heat load applied during one passing of the heat load, N is the total number of passings, τ_i describes a shift in time, and $\Psi_i(\mathbf{x}) : \mathbb{R}^n \to \mathbb{R}^n$ describes a translation over $\mathbf{x}_i \in \mathbb{R}^n$ followed by a rotation with rotation matrix $\mathbf{R}_i = \mathbf{R}_i^{-\top} \in \mathbb{R}^{n \times n}$, that is

$$\Psi_i : \mathbf{x} \mapsto \mathbf{R}_i(\mathbf{x} - \mathbf{x}_i). \quad (18)$$

Figure 2 illustrates the mapping $\Psi_i(\mathbf{x})$ for the wafer heating application in Figure 1 where $n = 2$. For this application, $Q_{\text{pass}}(\mathbf{x}, t)$ represents the heat load applied to a single field (one light blue rectangle in Figure 1) and the matrix $\mathbf{R}_i$ is completely characterized by one angle φ_i. It is most convenient to define $Q_{\text{pass}}(\mathbf{x}, t)$ as the heat load resulting from the scanning of a field in the positive x_2-direction that is centered at $\mathbf{x} = \mathbf{0}$. In that case, $\mathbf{x}_i = [x_{i,1}, x_{i,2}]^\top$ is the center of i-th field and $\varphi_i = 0$ when the field is scanned in the positive x_2-direction and $\varphi_i = \pi$ when the field is scanned in the negative x_2-direction.

Remark 3. In 3-D problems, the heat load is often described through a BC of the form $q_{\Omega,n}(\mathbf{x}, t) = q_{\partial\Omega}(\mathbf{x}, t)$ on $\mathbf{x} \in \partial\Omega$, where $q_{\partial\Omega}(\mathbf{x}, t) : \partial\Omega \times I \to \mathbb{R}$ is some prescribed heat load. Such heat loads at the boundary can also be incorporated in this framework because they are (in the weak sense) equivalent to an internal heat load $Q_\Omega(\mathbf{x}, t)$. For example, the heat load $\mathbf{q}_{\Omega,n}(\mathbf{x}, t) = q_{\partial\Omega}(\mathbf{x}, t)$ applied at the plane $x_1 = x_e$ is equivalent to the internal heat load $Q_\Omega(\mathbf{x}, t) = q(\mathbf{x}, t)\delta(x_1 - x_e)$.

Because (1a) is linear and translation, rotation, and time invariant on $\mathbb{R}^n$, the temperature field $T_{\Omega,\infty}(\mathbf{x}, t)$ resulting from zero ICs and a repetitive heat load $Q_{\Omega,\infty}(\mathbf{x}, t)$ of the form (17) can be written as

$$T_{\Omega,\infty}(\mathbf{x}, t) = \sum_{i=1}^{N} T_{\text{pass}}(\Psi_i(\mathbf{x}), t - \tau_i), \tag{19}$$

where $T_{\text{pass}}(\mathbf{x}, t) : \mathbb{R}^n \times ((-\infty, 0) \cup I) \to \mathbb{R}$ is zero for $t < 0$ and equal to the temperature field resulting from zero ICs and the heat load $Q_{\text{pass}}(\mathbf{x}, t) : \mathbb{R}^n \times I \to \mathbb{R}$ for $t \in I$.

The displacement field $\mathbf{u}_{\Omega,\infty}(\mathbf{x}, t) : \mathbb{R}^n \times I \to \mathbb{R}^n$ can be expressed similarly in terms of the displacement field $\mathbf{u}_{\text{pass}}(\mathbf{x}, t) : \mathbb{R}^n \times ((-\infty, 0) \cup I) \to \mathbb{R}^n$, the displacement field resulting from $T_{\text{pass}}(\mathbf{x}, t)$. However, it is important to note that rotations $\Psi_i(\mathbf{x})$ also rotate the local coordinate system in which $\mathbf{u}_{\text{pass}}(\Psi_i(\mathbf{x}), t)$ is expressed, see Figure 2. This also follows when considering the displacement potential $\psi_{\Omega,\infty}(\mathbf{x}, t)$ resulting from $T_{\Omega,\infty}(\mathbf{x}, t)$ according to (10). Since Equation (10) is linear and translation, rotation, and time invariant,

$$\psi_{\Omega,\infty}(\mathbf{x}, t) = \sum_{i=1}^{N} \psi_{\text{pass}}(\Psi_i(\mathbf{x}), t - \tau_i), \tag{20}$$

where $\psi_{\text{pass}}(\mathbf{x}, t) : \mathbb{R}^n \times ((-\infty, 0) \cup I) \to \mathbb{R}$ is the displacement field potential resulting from $T_{\text{pass}}(\mathbf{x}, t)$ according to (10). Differentiating both sides of (20) w.r.t. $\mathbf{x}$ shows that

$$\frac{\partial \psi_{\Omega,\infty}}{\partial \mathbf{x}}(\mathbf{x}, t) = \sum_{i=1}^{N} \frac{\partial \psi_{\text{pass}}}{\partial \mathbf{x}}(\Psi_i(\mathbf{x}), t - \tau_i)\mathbf{R}_i, \tag{21}$$

where it was used that $\Psi_i(\mathbf{x})$ is of the form (18). Because $\nabla = (\partial/\partial\mathbf{x})^\top$ in Cartesian coordinates and using (14), taking the transpose of (21) yields

$$\mathbf{u}_{\Omega,\infty}(\mathbf{x}, t) = \sum_{i=1}^{N} \mathbf{R}_i^\top \mathbf{u}_{\text{pass}}(\Psi_i(\mathbf{x}), t - \tau_i). \tag{22}$$

The rotation matrices $\mathbf{R}_i$ thus indeed appear in the construction of $\mathbf{u}_{\Omega,\infty}(\mathbf{x}, t)$, as is also illustrated in Figure 2.

Note that it is often much easier to compute $T_{\text{pass}}(\mathbf{x}, t)$ and $\mathbf{u}_{\text{pass}}(\mathbf{x}, t)$ resulting from $Q_{\text{pass}}(\mathbf{x}, t)$ than the solution $\mathbf{u}_{\Omega,\infty}(\mathbf{x}, t)$ resulting from $Q_{\Omega,\infty}(\mathbf{x}, t)$ because $\mathbf{u}_{\text{pass}}(\mathbf{x}, t)$ typically needs to be computed over a smaller time window and requires a mesh of a smaller part of the spatial domain than $\mathbf{u}_{\Omega,\infty}(\mathbf{x}, t)$. This makes the construction of $T_{\Omega,\infty}(\mathbf{x}, t)$ and $\mathbf{u}_{\Omega,\infty}(\mathbf{x}, t)$ through (19) and (22) attractive in many applications such as the wafer heating problem considered in Section 5.

The problem remains to convert the temperature and displacement fields $T_{\Omega,\infty}(\mathbf{x}, t)$ and $\mathbf{u}_{\Omega,\infty}(\mathbf{x}, t)$ on $\mathbb{R}^n$ to solutions $T_{\Omega}(\mathbf{x}, t)$ and $\mathbf{u}_{\Omega}(\mathbf{x}, t)$ on the subdomain $\Omega \subset \mathbb{R}^n$ of interest. This can be accomplished by the MoI that will be introduced in the following section.

Remark 4. Another motivation for the study of the MoI is that many (semi-)analytic methods such as [4, 5, 11, 17] are most conveniently developed on $\mathbb{R}^n$ because the temperature field $T_{\Omega,\infty}(\mathbf{x}, t)$ (with zero ICs) can be expressed as [2]

$$T_{\Omega,\infty}(\mathbf{x}, t) = \int_0^t \iint_{\mathbb{R}^n} \Phi(\mathbf{x} - \mathbf{x}', t - \tau) Q_{\Omega,\infty}(\mathbf{x}', \tau) d\mathbf{x}' \, d\tau, \tag{23a}$$

where $\Phi(\mathbf{x}, t)$ denotes the fundamental solution of the heat equation

$$\Phi(\mathbf{x}, t) = \sqrt{\frac{c^n}{(4\pi\kappa t)^n}} \exp\left(\frac{-c\|\mathbf{x}\|^2}{4\kappa t}\right). \tag{23b}$$
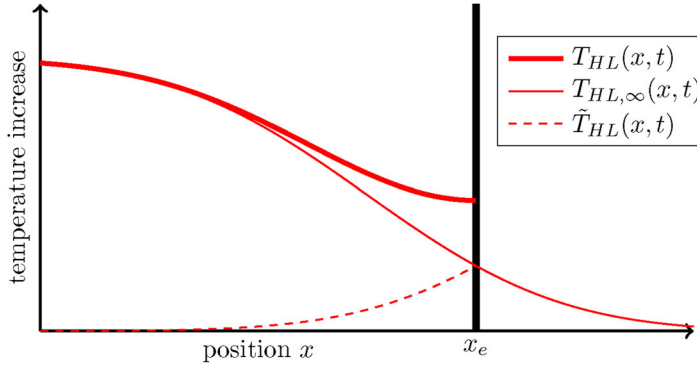
Figure 3. The MoI on the half line $HL = \{x \in \mathbb{R} \mid x \leq x_e\}$.

The MoI enables the application of these methods to certain subdomains $\Omega \subset \mathbb{R}^n$ as well.

3. The method of images

3.1. A Kernel representation

The kernel representation for the MoI is best understood from the following example.

Example 1. Consider the heat conduction problem (1a) on a one-dimensional spatial domain, that is $n = 1$. The spatial coordinate is denoted by $x \in \mathbb{R}$ and the spatial domain of interest is the half line $HL = \{x \in \mathbb{R} \mid x < x_e\}$. The boundary is perfectly insulated, that is $\partial T_{HL}/\partial x = 0$ at $x = x_e$ (Neumann BC). The MoI now provides a way to construct the solution $T_{HL}(x, t) : HL \times I \to \mathbb{R}$ resulting from a heat load $Q_{HL}(x, t) : HL \times I \to \mathbb{R}$ and zero ICs based on the solution $T_{HL,\infty}(x, t) : \mathbb{R} \times I \to \mathbb{R}$ resulting from a heat load $Q_{HL,\infty}(x, t) : \mathbb{R} \times I \to \mathbb{R}$ defined according to (16) and zero ICs, see also Figure 3. To see how this can be done, consider $\tilde{T}_{HL}(x, t) : HL \times I \to \mathbb{R}$,

$$\tilde{T}_{HL}(x, t) = T_{HL}(x, t) - T_{HL,\infty}(x, t), \tag{24a}$$

that is the difference between the desired solution $T_{HL}(x, t)$ and the restriction of $T_{HL,\infty}(x, t)$ to HL. As $T_{HL}(x, t)$ and $T_{HL,\infty}(x, t)$ are both solutions of (1a), $\tilde{T}_{HL}(x, t)$ is a solution of (1a) with $Q_{HL}(x, t) \equiv 0$ that satisfies the BC $\partial \tilde{T}_{HL}/\partial x = -\partial T_{HL,\infty}/\partial x$ at $x = x_e$ and zero ICs.

The restriction of $T_{HL,\infty}(x, t)$ to $HL^c = \mathbb{R} \, HL$ is also a solution of (1a) with $Q_{HL}(x, t) \equiv 0$ due to the definition of $Q_{HL,\infty}(x, t)$ in (16). Because $2x_e - x \in HL^c$ iff $x \in HL$, it is easy to verify that $T_{HL,\infty}(2x_e - x, t)$ is a solution of (1a) with $Q_{HL}(x, t) \equiv 0$ on $x \in HL$. We conclude that

$$\tilde{T}_{HL}(x, t) = T_{HL,\infty}(2x_e - x, t), \tag{24b}$$

because the expression for $\tilde{T}_{HL}(x, t)$ in (24b) also satisfies the BC $\partial \tilde{T}_{HL}/\partial x = -\partial T_{HL,\infty}/\partial x$ at $x = x_e$ and zero ICs. In other words, the solution $\tilde{T}_{HL}(x, t)$ can be found by mirroring the restriction of $T_{HL,\infty}(x, t)$ to HL^c in the edge $x = x_e$. This is also illustrated in Figure 3.

Remark 5. The name 'Method of Images' originates from the observation that $T_{HL,\infty}(2x_e - x, t) : \mathbb{R} \times I \to \mathbb{R}$ is the solution resulting from the heat load $Q_{HL,\infty}(2x_e - x, t) : \mathbb{R} \times I \to \mathbb{R}$. The temperature field $T_{HL}(x, t)$ in (24a) can thus also be considered as the sum of the truncation of the temperature field resulting from $Q_{HL,\infty}(x, t)$ and its mirror image $Q_{HL,\infty}(2x_e - x, t)$.

Remark 6. Instead of the Neumann BC $\partial T_{HL}/\partial x = 0$ at $x = x_e$, also a Dirichlet BC $T(x_e, t) = 0$ or a Robin BC $aT_{HL} + \partial T_{HL}/\partial x = 0$ at $x = x_e$ with $a > 0$ could have been considered in Example 1.

For these two BCs, the T_{HL} can still be expressed in the form (24a), but (24b) should then be replaced by

$$\tilde{T}_{HL}(x,t) = -T_{HL,\infty}(2x_e - x, t) \tag{25}$$

$$\tilde{T}_{HL}(x,t) = T_{HL,\infty}(2x_e - x, t) - 2a \int_0^\infty e^{-ax'} T_{HL,\infty}(2x_e - x + x', t) \, \mathrm{d}x', \tag{26}$$

respectively. It is easy to see that (26) approaches (24b) for $a \to 0$. With a little more effort it can be shown that (26) approaches (25) for $a \to \infty$ as well.

It is now attempted to generalize the construction of $T_{HL}(x,t)$ on a one-dimensional spatial domain in Example 1 to n-dimensional spatial domains Ω. The problem is thus to obtain an expression for the temperature field $T_\Omega(\mathbf{x},t) : \Omega \times I \to \mathbb{R}$ on a spatial domain $\Omega \subset \mathbb{R}^n$ resulting from a heat load $Q_\Omega(\mathbf{x},t) : \Omega \times I \to \mathbb{R}$ with BCs (6a) and zero ICs in terms of the solution $T_{\Omega,\infty}(\mathbf{x},t) : \mathbb{R}^n \times I \to \mathbb{R}$ resulting from the heat load $Q_{\Omega,\infty}(\mathbf{x},t) : \mathbb{R}^n \times I \to \mathbb{R}$ as defined in (16) and zero ICs. The derivation presented here considers the most commonly used zero Neumann BC (6a), but can be easily adapted to zero Dirichlet and Robin BCs, see also Remark 7 later on. Similar to the 1-D case in (24a), it is useful to write

$$T_\Omega(\mathbf{x},t) = T_{\Omega,\infty}(\mathbf{x},t) + \tilde{T}_\Omega(\mathbf{x},t), \tag{27a}$$

where $\tilde{T}_\Omega(\mathbf{x},t) : \Omega \times I \to \mathbb{R}$ has thus been introduced as the difference between the desired solution $T_\Omega(\mathbf{x},t)$ and the restriction of $T_{\Omega,\infty}(\mathbf{x},t)$ to Ω. Because both $T_\Omega(\mathbf{x},t)$ and $T_{\Omega,\infty}(\mathbf{x},t)$ are solutions of (1a) and in view of the Neumann BC (6a), $\tilde{T}_\Omega(\mathbf{x},t)$ should satisfy

$$c \frac{\partial \tilde{T}_\Omega}{\partial t} = \kappa \nabla^2 \tilde{T}_\Omega - h_0 \tilde{T}_\Omega, \qquad \text{on } \Omega \times I, \tag{27b}$$

$$\nabla \tilde{T}_\Omega \cdot \mathbf{n} = -\nabla T_{\Omega,\infty} \cdot \mathbf{n}, \qquad \text{on } \partial\Omega \times I, \tag{27c}$$

and zero ICs. The definition of $Q_{\Omega,\infty}(\mathbf{x},t)$ in (16) implies that the restriction of $T_{\Omega,\infty}(\mathbf{x},t)$ to $\Omega^c := \mathbb{R}^n \, \Omega$ is also a solution of (1a) with $Q_\Omega \equiv 0$. It is therefore attempted to express $\tilde{T}_\Omega(\mathbf{x},t)$ in terms of the restriction of $T_{\Omega,\infty}(\mathbf{x},t)$ to Ω^c through a convolution kernel $\omega_\Omega : \Omega \times \Omega^c \to \mathbb{R}$, that is

$$\tilde{T}_\Omega(\mathbf{x},t) = \iint_{\Omega^c} \omega_\Omega(\mathbf{x},\mathbf{x}') \tilde{T}(\mathbf{x}',t) \mathrm{d}\mathbf{x}'. \tag{27d}$$

The following proposition gives conditions on the kernel $\omega_\Omega(\mathbf{x},\mathbf{x}')$ for which $\tilde{T}_\Omega(\mathbf{x},t)$ in (27d) is indeed the solution of (27b)–(27c), that is, conditions for which inserting (27d) into (27a) indeed yields the solution $T_\Omega(\mathbf{x},t)$ of (1a) with the BC (6a) and zero ICs.

Proposition 1. *The function $\tilde{T}_\Omega(\mathbf{x},t)$ in (27d) satisfies (27b)–(27c) if the kernel $\omega_\Omega : \Omega \times \Omega^c \to \mathbb{R}$ satisfies*

$$\nabla'^2 \omega_\Omega(\mathbf{x},\mathbf{x}') = \nabla^2 \omega_\Omega(\mathbf{x},\mathbf{x}'), \tag{28a}$$

for $\mathbf{x} \in \Omega, \mathbf{x}' \in \Omega^c$,

$$\omega_\Omega(\mathbf{x},\mathbf{x}') = \nabla' \omega_\Omega(\mathbf{x},\mathbf{x}') \cdot \mathbf{n}(\mathbf{x}') = 0, \tag{28b}$$

for $\mathbf{x} \in \Omega, \mathbf{x}' \in \partial\Omega$

$$\nabla \omega_\Omega(\mathbf{x},\mathbf{x}') \cdot \mathbf{n}(\mathbf{x}) = \nabla' \delta(\mathbf{x} - \mathbf{x}') \cdot \mathbf{n}(\mathbf{x}), \tag{28c}$$

for $\mathbf{x} \in \partial\Omega, \mathbf{x}' \in \Omega^c$.

Here, ∇' and ∇'^2 denote the gradient and Laplacian w.r.t. $\mathbf{x}'$. Note that this result involves the gradient of the Dirac delta in (28c) which should be interpreted in the weak sense, that is, for any $\Omega' \subseteq \mathbb{R}^n$ and any smooth function $f : \Omega' \to \mathbb{R}$

$$\iint_{\Omega'} f(\mathbf{x}') \nabla' \delta(\mathbf{x}') d\mathbf{x}' = -\iint_{\Omega'} \left(\nabla' f(\mathbf{x}') \right) \delta(\mathbf{x}') d\mathbf{x}'. \tag{29}$$

The proof of Proposition 1 can be found in Appendix A.

Remark 7. For the Dirichlet BC $T_\Omega(\mathbf{x}, t) = 0$ on $\mathbf{x} \in \partial\Omega$, (27c) changes to

$$\tilde{T}_\Omega(\mathbf{x}, t) = -T_{\Omega, \infty}(\mathbf{x}, t), \tag{30a}$$

on $(\mathbf{x}, t) \in \partial\Omega \times I$ and (28c) should be replaced by

$$\omega_\Omega(\mathbf{x}, \mathbf{x}') = -\delta(\mathbf{x} - \mathbf{x}'), \tag{30b}$$

for $\mathbf{x} \in \partial\Omega$ and $\mathbf{x}' \in \Omega^c$. For the Robin BC $aT_\Omega(\mathbf{x}, t) + \nabla T_\Omega(\mathbf{x}, t) \cdot \mathbf{n}(\mathbf{x}) = 0$ with $a > 0$, (27c) changes to

$$a\tilde{T}_\Omega(\mathbf{x}, t) + \nabla \tilde{T}_\Omega(\mathbf{x}, t) \cdot \mathbf{n}(\mathbf{x}) = -aT_{\Omega, \infty}(\mathbf{x}, t) - \nabla T_{\Omega, \infty}(\mathbf{x}, t) \cdot \mathbf{n}(\mathbf{x}), \tag{31a}$$

on $(\mathbf{x}, t) \in \partial\Omega \times I$ and (28c) should be replaced by

$$a\omega_\Omega(\mathbf{x}, \mathbf{x}') + \nabla \omega_\Omega(\mathbf{x}, t) \cdot \mathbf{n}(\mathbf{x}) = -a\delta(\mathbf{x} - \mathbf{x}') + \nabla' \delta(\mathbf{x} - \mathbf{x}') \cdot \mathbf{n}(\mathbf{x}), \tag{31b}$$

for $\mathbf{x} \in \partial\Omega$ and $\mathbf{x}' \in \Omega^c$.

Remark 8. An equation of the form (28a) is called ultrahyperbolic. When $n = 2$, so when $\omega_\Omega(\mathbf{x}, \mathbf{x}')$ depends on four variables, (28a) is also known as John's equation [24]. There is a correspondence between solutions of (28a) with $n = 2$ and functions $\mathbb{R}^3 \to \mathbb{R}$ through the Radon transform and a mapping from the lines in $\mathbb{R}^3$ to points in $\mathbb{R}^4$ [24]. This idea can be generalized for $n > 2$ [25]. For a general domain Ω, it cannot be guaranteed that there exists a kernel $\omega_\Omega(\mathbf{x}, \mathbf{x}')$ that satisfies (28) [24, 25].

Although the existence of solutions $\omega_\Omega(\mathbf{x}, \mathbf{x}')$ of the ultrahyperbolic problem (28) cannot be guaranteed in general, it is often easy to determine the kernel $\omega_\Omega(\mathbf{x}, \mathbf{x}')$ from formulas available in the literature. This is demonstrated by the following example.

Example 1 (Continued). Consider again the half line $HL = \{x \in \mathbb{R} \mid x < x_e\}$ with a perfectly insulated BC $\partial T_{HL}/\partial x = 0$ at $x = x_e$ from Example 1. As the formula for $\tilde{T}_{HL}(x, t)$ is given in (24b), it easy to see from (27d) that

$$\omega_{HL}(x, x') = \delta(2x_e - x - x'). \tag{32}$$

One can easily verify that this kernel indeed satisfies the conditions in (28).

The kernel $\omega_{HL}(x, x')$ can also be found from the conditions (28). The solution of the 1-D wave Equation (28a) with propagation speed 1 is given by d'Alembert's formula, see for example [2],

$$\begin{aligned} \omega_{HL}(x, x') &= F_+((x - x_e) - (x' - x_e)) + F_-((x - x_e) + (x' - x_e)) \\ &= F_+(x - x') + F_-(x + x' - 2x_e), \end{aligned} \tag{33a}$$

where $F_+(\xi) : \mathbb{R} \to \mathbb{R}$ and $F_-(\xi) : \mathbb{R} \to \mathbb{R}$ are the positive- and negative-going wave, respectively. Because $x \in HL$, that is $x < x_e$, and $x' \in HL^c := \mathbb{R} \backslash HL$, it follows that $x' > x_e$ and the values of

$F_+(\xi)$ only influence $\omega(x, x')$ for $\xi < 0$. Furthermore, the zero ICs (28b) imply that $F_+(\xi) = F_-(\xi) = 0$ for $\xi < 0$. It thus follows that

$$\omega_{HL}(x, x') = F_-(x + x' - 2x_e). \tag{33b}$$

To determine $F_-(\xi)$ for $\xi \geq 0$, (33b) is inserted in (28c)

$$\frac{\partial F_-}{\partial \xi}(\xi) = \frac{\partial \delta}{\partial \xi}(\xi), \tag{33c}$$

where $\xi = x + x' - 2x_e$. The solution of (33c) is clearly of the form $F_-(\xi) = \delta(\xi) + C$, for some constant C. As $F_-(\xi) = 0$ for $\xi < 0$, C must be zero so that $F_-(\xi) = \delta(\xi)$. Inserting this result into (33b) and using that $\xi = x + x' - 2x_e$ yields (32).

In other cases, the number of independent variables $(\mathbf{x}, \mathbf{x}')$ on which ω_Ω depends can be reduced based on certain symmetries of the spatial domain Ω. It is then often possible to reduce the ultrahyperbolic Equation (28a) to a hyperbolic equation for which the existence and uniqueness of solutions is well understood, see for example [2]. This approach will be used in several examples in Section 4.

3.2. Heat-induced deformation

The reformulation of the MoI in terms of a convolution kernel $\omega_\Omega(\mathbf{x}, \mathbf{x}')$ so far only considered the temperature field $T_\Omega(\mathbf{x}, t)$ in the thermal model (1a). The displacement field $\mathbf{u}_\Omega(\mathbf{x}, t)$ in the mechanical model (1b) will be considered now.

The extension of the MoI is based on the decomposition of $\mathbf{u}_\Omega(\mathbf{x}, t)$ into $\mathbf{u}_\Omega^{(T)}(\mathbf{x}, t)$ and $\mathbf{u}_\Omega^{(BC)}(\mathbf{x}, t)$ as in (7a). The part $\mathbf{u}_\Omega^{(T)}(\mathbf{x}, t)$ is the gradient of a displacement potential $\psi_\Omega(\mathbf{x}, t)$ that satisfies (10) and is a particular solution of (1b) for the given temperature field $T_\Omega(\mathbf{x}, t)$. Because (10) is linear, the displacement potential $\psi_\Omega(\mathbf{x}, t) : \Omega \times I \to \mathbb{R}$ is constructed in a similar manner as $T_\Omega(\mathbf{x}, t)$ in (27a) and (27d)

$$\psi_\Omega(\mathbf{x}, t) = \psi_{\Omega, \infty}(\mathbf{x}, t) + \tilde{\psi}_\Omega(\mathbf{x}, t), \tag{34a}$$

$$\tilde{\psi}_\Omega(\mathbf{x}, t) = \iint_{\Omega^c} \omega_\Omega(\mathbf{x}, \mathbf{x}') \psi_{\Omega, \infty}(\mathbf{x}', t) d\mathbf{x}', \tag{34b}$$

where $\omega_\Omega(\mathbf{x}, \mathbf{x}')$ is the same as in (27d) and $\psi_{\Omega, \infty}(\mathbf{x}, t) : \mathbb{R}^n \times I \to \mathbb{R}$ is the displacement potential that satisfies (10) with $T_\Omega(\mathbf{x}, t) \equiv T_{\Omega, \infty}(\mathbf{x}, t)$. Recall that $\psi_{\Omega, \infty}(\mathbf{x}, t)$ is unique when $k_0 > 0$.

Note that substitution of (27a) and (34a) into (10) shows that $\tilde{\psi}_\Omega(\mathbf{x}, t)$ should be the displacement potential resulting from $\tilde{T}_\Omega(\mathbf{x}, t)$, that is, $\tilde{\psi}_\Omega(\mathbf{x}, t)$ should satisfy (10) with $T_\Omega(\mathbf{x}, t) = T_{\Omega, \infty}(\mathbf{x}, t)$. The following result shows that (34b) indeed defines a displacement potential $\tilde{\psi}_\Omega(\mathbf{x}, t)$ resulting from $\tilde{T}(\mathbf{x}, t)$ in (27d) and that $\tilde{\psi}_\Omega(\mathbf{x}, t)$ inherits certain BCs from the thermal problem.

Lemma 1. *Assume that the kernel $\omega_\Omega(\mathbf{x}, \mathbf{x}')$ satisfies the conditions in (28) and that $\tilde{T}_\Omega(\mathbf{x}, t)$ is defined as in (27d). Let $\psi_{\Omega, \infty}(\mathbf{x}, t)$ be a solution of (10) with $T_\Omega(\mathbf{x}, t) \equiv T_{\Omega, \infty}(\mathbf{x}, t)$, then the function $\tilde{\psi}_\Omega(\mathbf{x}, t)$ in (34b) satisfies*

$$(2\mu + \lambda)\nabla^2 \tilde{\psi}_\Omega - \tilde{k}_0 \tilde{\psi}_\Omega = (2\mu + n\lambda)\alpha \tilde{T}_\Omega, \tag{35a}$$

on $\Omega \times I$ and

$$\nabla \tilde{\psi}_\Omega \cdot \mathbf{n} = -\nabla \psi_{\Omega, \infty} \cdot \mathbf{n}, \tag{35b}$$

on $\partial\Omega \times I$.

The proof of Lemma 1 can be found in Appendix A.

Because the displacement potential is typically not of interest itself, it is most insightful to first construct the displacement potential $\psi_\Omega(\mathbf{x}, t)$ according to (34) and then compute the resulting displacement field $\mathbf{u}_\Omega(\mathbf{x}, t)$ according to (7b). This is illustrated by the following example.

Example 1 (Continued). Consider once again the 1-D spatial domain $\Omega = \{x \in \mathbb{R} \mid x < x_e\}$ with a perfectly insulated (Neumann) BC $\partial T_{HL}/\partial x = 0$ at $x = x_e$ from Example 1. As the kernel $\omega_{HL}(x, x')$ is given by (32), a displacement potential $\psi_{HL}(x, t)$ for this problem follows from (34) as

$$\psi_{HL}(x, t) = \psi_{HL, \infty}(x, t) + \psi_{HL, \infty}(2x_e - x, t). \tag{36a}$$

By taking the gradient of (36a) and using (7b) and (14), an expression for the corresponding (scalar-valued) displacement field $u_{HL}^{(T)}(x, t)$ is obtained as

$$u_{HL}^{(T)}(x, t) = u_{HL, \infty}(x, t) - u_{HL, \infty}(2x_e - x, t). \tag{36b}$$

It is easy to see from (36b) that $u_{HL}^{(T)}(x, t) = 0$ on the edge $x = x_e$. This observation generalizes to higher dimensions $n > 1$ as follows. By differentiating (34a) and using (35b), it follows that

$$\nabla \psi_\Omega(\mathbf{x}, t) \cdot \mathbf{n}(\mathbf{x}) = 0, \qquad \mathbf{x} \in \partial\Omega, t \in I. \tag{37a}$$

Using (7b), this result can be rewritten as

$$\mathbf{u}_\Omega^{(T)}(\mathbf{x}, t) \cdot \mathbf{n}(\mathbf{x}) = 0, \qquad \mathbf{x} \in \partial\Omega, t \in I, \tag{37b}$$

which shows that the component normal to the edge of displacement field $\mathbf{u}_\Omega^{(T)}(\mathbf{x}, t)$ is zero.

Remark 9. A similar result can be obtained for Dirichlet BCs. To obtain the temperature field $T_\Omega(\mathbf{x}, t)$ such that the Dirichlet BC $T_\Omega(\mathbf{x}, t) = 0$ for $\mathbf{x} \in \partial\Omega$ is satisfied, the kernel $\omega_\Omega(\mathbf{x}, \mathbf{x}')$ should satisfy (30b) instead of (28c). For this case, it is easy to see from (34b) and (30b) that $\tilde{\psi}_\Omega(\mathbf{x}, t) = -\psi_{\Omega, \infty}(\mathbf{x}, t)$ for $\mathbf{x} \in \partial\Omega$, so that (34a) shows that $\psi_\Omega(\mathbf{x}, t) = 0$ for $\mathbf{x} \in \partial\Omega$. This implies that the gradient of $\psi_\Omega(\mathbf{x}, t)$ in all directions parallel to the edge will be zero, that is for all $\mathbf{v} \in \mathbb{R}^n$ that satisfy $\mathbf{v} \cdot \mathbf{n}(\mathbf{x}) = 0$ at a point $\mathbf{x} \in \partial\Omega$

$$\nabla \psi_\Omega(\mathbf{x}, t) \cdot \mathbf{v} = \mathbf{u}_\Omega^{(T)}(\mathbf{x}, t) \cdot \mathbf{v} = 0. \tag{38}$$

All components of $\mathbf{u}_\Omega^{(T)}(\mathbf{x}, t)$ along the edge are thus zero on $\partial\Omega$ when the kernel $\omega_\Omega(\mathbf{x}, \mathbf{x}')$ is constructed such that $T_\Omega(\mathbf{x}, t)$ satisfies zero Dirichlet BCs.

Recall that the displacement field $\mathbf{u}_\Omega(\mathbf{x}, t)$ is decomposed into the two parts $\mathbf{u}_\Omega^{(T)}(\mathbf{x}, t)$ and $\mathbf{u}_\Omega^{(BC)}(\mathbf{x}, t)$. The presented extension of the MoI to thermomechanical systems only considers the part $\mathbf{u}_\Omega^{(T)}(\mathbf{x}, t) = \nabla \psi_\Omega(\mathbf{x}, t)$, which is a good approximation of $\mathbf{u}_\Omega(\mathbf{x}, t)$ away from the edge $\partial\Omega$. The part $\mathbf{u}_\Omega^{(BC)}(\mathbf{x}, t)$ is the solution of the standard elasticity problem (11) in which $\mathbf{u}_\Omega^{(T)}(\mathbf{x}, t)$ appears in the BCs, see for example (12). When the spatial domain Ω is large enough, as in the wafer heating application in Section 5, the solution $\mathbf{u}_\Omega^{(BC)}(\mathbf{x}, t)$ is concentrated near the edge $\partial\Omega$ and can be computed much easier than $\mathbf{u}_\Omega(\mathbf{x}, t)$.

4. The method of images for specific domains

4.1. Orthogonal domains

The examples in this subsection demonstrate how the conditions (28) can be used to determine the convolution kernel $\omega_\Omega(\mathbf{x}, \mathbf{x}')$ for several orthogonal domains Ω. When the kernel has been found, expressions for the temperature field $T_\Omega(\mathbf{x}, t)$ and the displacement potential $\psi_\Omega(\mathbf{x}, t)$ and the corresponding displacement field $\mathbf{u}_\Omega^{(T)}(\mathbf{x}, t)$ in terms of the infinite domain solutions $T_{\Omega, \infty}(\mathbf{x}, t)$, $\psi_{\Omega, \infty}(\mathbf{x}, t)$, and $\mathbf{u}_{\Omega, \infty}^{(T)}(\mathbf{x}, t)$ follow easily. The expressions for the temperature field

$T_\Omega(\mathbf{x}, t)$ on the orthogonal domains Ω considered in this section can also be found in the literature, see for example [1, 5], but the expressions for the kernel $\omega_\Omega(\mathbf{x}, \mathbf{x}')$, the displacement potential $\psi_\Omega(\mathbf{x}, t)$, and the displacement field $\mathbf{u}_\Omega^{(T)}(\mathbf{x}, t)$ are novelties.

The first two examples are extensions of Example 1 to the 2-D half plane and the 3-D half space.

Example 2 (2-D half plane). Consider the 2-D half plane $HP = \{\mathbf{x} \in \mathbb{R}^2 \mid x_1 < x_e\}$. As the spatial domain is invariant under translations in the x_2-direction,

$$\omega_{HP}(x_1, x_2, x_1', x_2') = \omega_{HP}(x_1, x_2 - x_2', x_1'). \tag{39}$$

By introducing $\hat{x} := x_2 - x_2'$, conditions (28) become

$$\frac{\partial^2 \omega_{HP}}{\partial x_1'^2}(x_1, \hat{x}, x_1') = \frac{\partial^2 \omega_{HP}}{\partial x_1^2}(x_1, \hat{x}, x_1'), \tag{40a}$$

$$\omega_{HP}(x_1, \hat{x}, x_e) = \frac{\partial \omega_{HP}}{\partial x_1'}(x_1, \hat{x}, x_e) = 0, \tag{40b}$$

$$\frac{\partial \omega_{HP}}{\partial x_1}(x_e, \hat{x}, x') = \frac{\partial \delta}{\partial x_1}(x_e - x_1')\delta(\hat{x}), \tag{40c}$$

where $x_1 < x_e$ and $x_1' > x_e$. Note that (40c) follows because $\delta(\mathbf{x} - \mathbf{x}') = \delta(x_1 - x_1')\delta(x_2 - x_2')$ when $n = 2$. By considering $(x_1, \hat{x})$ as the 'spatial' variables and x_1' as the 'temporal' variable, (40) can be viewed as a wave equation. In particular, (40a) shows that the propagation speed equals 1, (40b) shows that the ICs at $x_1' = x_e$ are zero, and (40c) shows there is an input at the boundary $x_1 = x_e$. By considering the weak form of (40), it is shown in Appendix B.1 that (40b) and (40c) are equivalent to

$$\lim_{\varepsilon \downarrow 0} \omega_{HP}(x_1, \hat{x}, x_e + \varepsilon) = \delta(x_1 - x_e)\delta(\hat{x}), \tag{41a}$$

$$\lim_{\varepsilon \downarrow 0} \frac{\partial \omega_{HP}}{\partial x_1'}(x_1, \hat{x}, x_e + \varepsilon) = 0, \tag{41b}$$

$$\frac{\partial \omega_{HP}}{\partial x_1}(x_e, \hat{x}, x_1') = 0, \tag{41c}$$

for $x_1' > x_e$. One easily verifies that the solution of (40a) with ICs (41a) and (41b) and the BC (41c) is a Dirac delta traveling in the negative x_1-direction, that is

$$\omega_{HP}(x_1, \hat{x}, x_1') = \delta(2x_e - x_1 - x_1')\delta(\hat{x}). \tag{42}$$

Inserting (42) into (27d) and using (27a) now yields

$$T_{HP}(\mathbf{x}, t) = T_{HP,\infty}(\mathbf{x}, t) + T_{HP,\infty}(\mathbf{x}_I, t), \tag{43}$$

where $\mathbf{x}_I$ denotes the mirror image of $\mathbf{x}$ in the edge $x_1 = x_e$, that is, $\mathbf{x}_I = [2x_e - x_1, x_2]^\top$. Furthermore, inserting (42) into (34b) and using (34a) shows that

$$\psi_{HP}(\mathbf{x}, t) = \psi_{HP,\infty}(\mathbf{x}, t) + \psi_{HP,\infty}(\mathbf{x}_I, t). \tag{44}$$

Taking the gradient of (44) and using (14) yields

$$\begin{bmatrix} u_{HP,1}^{(T)}(\mathbf{x}, t) \\ u_{HP,2}^{(T)}(\mathbf{x}, t) \end{bmatrix} = \begin{bmatrix} u_{HP,\infty,1}(\mathbf{x}, t) - u_{HP,\infty,1}(\mathbf{x}_I, t) \\ u_{HP,\infty,2}(\mathbf{x}, t) + u_{HP,\infty,2}(\mathbf{x}_I, t) \end{bmatrix}. \tag{45}$$

Observe that the formulas for the 1- and 2-components of $\mathbf{u}_{HP}^{(T)}(\mathbf{x}, t)$ are different. It is also easy to verify that $u_{HP,1}^{(T)}(\mathbf{x}, t) = 0$ at $x_1 = x_e$, which is in agreement with (37). Finally, note that inserting (45) into the (1, 2) shear stress component of $\boldsymbol{\sigma}(\mathbf{x}, t)$ in (5b) shows that

$$\sigma_{HP,12}^{(T)}(\mathbf{x},t) = \mu\left(\frac{\partial u_{HP,\infty,1}}{\partial x_2}(\mathbf{x},t) - \frac{\partial u_{HP,\infty,1}}{\partial x_2}(\mathbf{x}_I,t) + \frac{\partial u_{HP,\infty,2}}{\partial x_1}(\mathbf{x},t) - \frac{\partial u_{HP,\infty,2}}{\partial x_1}(\mathbf{x}_I,t)\right), \quad (46)$$

so that $\sigma_{HP,12}^{(T)}(\mathbf{x},t) = 0$ at the edge $x_1 = x_e$ where $\mathbf{x} = \mathbf{x}_I$. The displacement field in (45) is thus a solution of (1b) satisfying the BCs $u_{HP,1}^{(T)}(\mathbf{x},t) = 0$ and $\sigma_{HP,12}^{(T)}(\mathbf{x},t) = 0$.

Example 3 (3-D half space). The 3-D half space $HS = \{\mathbf{x} \in \mathbb{R}^3 \mid x_1 < x_e\}$ can be treated similarly as the 2-D half space in Example 2. By exploiting the translation-invariance in the x_2- and x_3-directions, one easily sees that conditions (28) can be reduced to a wave equation in the 'spatial' coordinates $(x_1, \hat{x}_1, \hat{x}_2) = (x_1, x_2 - x_2', x_3 - x_3')$ and temporal variable x_1'. The solution of this equation is again a Dirac delta traveling in the negative x_1-direction

$$\omega_{HS} = \delta(2x_e - x_1 - x_1')\delta(\hat{x}_2)\delta(\hat{x}_3). \quad (47)$$

The resulting temperature field and displacement potential thus become

$$T_{HS}(\mathbf{x},t) = T_{HS,\infty}(\mathbf{x},t) + T_{HS,\infty}(\mathbf{x}_I,t), \quad (48)$$

$$\psi_{HS}(\mathbf{x},t) = \psi_{HS,\infty}(\mathbf{x},t) + \psi_{HS,\infty}(\mathbf{x}_I,t), \quad (49)$$

where $\mathbf{x}_I = [2x_e - x_1, x_2, x_3]^\top$ denotes the mirror image of $\mathbf{x}$ in the plane $x_1 = x_e$. The displacement field $\mathbf{u}_\Omega^{(T)}(\mathbf{x},t)$ follows by taking the gradient of the displacement potential $\psi_{HS}(\mathbf{x},t)$ in (49)

$$\begin{bmatrix} u_{HS,1}^{(T)}(\mathbf{x},t) \\ u_{HS,2}^{(T)}(\mathbf{x},t) \\ u_{HS,3}^{(T)}(\mathbf{x},t) \end{bmatrix} = \begin{bmatrix} u_{HS,\infty,1}(\mathbf{x},t) - u_{HS,\infty,1}(\mathbf{x}_I,t) \\ u_{HS,\infty,2}(\mathbf{x},t) + u_{HS,\infty,2}(\mathbf{x}_I,t) \\ u_{HS,\infty,3}(\mathbf{x},t) + u_{HS,\infty,3}(\mathbf{x}_I,t) \end{bmatrix}. \quad (50)$$

Similarly as in Example 2, it can be verified that the displacememt field component $u_{HS,1}^{(T)}(\mathbf{x},t)$ and the shear components $\sigma_{HS,12}^{(T)}(\mathbf{x},t)$ and $\sigma_{HS,13}^{(T)}(\mathbf{x},t)$ vanish on the boundary $x_1 = x_e$.

Next, 1-D and 2-D domains with opposing parallel boundaries are considered.

Example 4 (The interval). Consider the interval $J = \{x \in \mathbb{R} \mid x_- < x < x_+\}$. When interpreting the condition (28a) for the kernel $\omega_J(x,x')$ again as a wave equation with x as the 'spatial' coordinate and x' as the 'temporal' coordinate, one observes that the 'temporal' domain $J^c = \mathbb{R}\backslash J$ is not connected. The solution $\omega_J(x,x')$ can therefore be obtained by combining the solutions $\omega_J^+(x,x')$ and $\omega_J^-(x,x')$ on the two connected parts $J_+^c = \{x' \in \mathbb{R} \mid x' \geq x_+\}$ and $J_-^c = \{x' \in \mathbb{R} \mid x' \leq x_-\}$ of J^c. Considering the weak form of the conditions (28) on $(x,x') \in J \times [x_+, x_+ + \varepsilon]$ similarly as in Appendix B.1, it can be shown that (28b) and (28c) are equivalent to

$$\omega_J^+(x,x_+) = \delta(x - x_+), \qquad \frac{\partial \omega_J^+}{\partial x'}(x,x_+) = 0, \quad (51a)$$

$$\frac{\partial \omega_J^+}{\partial x}(x_-,x') = 0, \qquad \frac{\partial \omega_J^+}{\partial x}(x_+,x') = 0, \quad (51b)$$

for $x \in J$ and $x' > x_+$. At the initial 'time' $x' = x_+$, $\omega_J^+(x, x')$ is thus a Dirac delta which travels with velocity 1 in the negative x-direction. At 'time' $x' = x_+ + (x_+ - x_-)$, the pulse reaches the boundary $x = x_-$ from which it is reflected. At 'time' $x' = x_+ + 2(x_+ - x_-)$ the pulse arrives again at $x = x_+$ where it reflected again and the process repeats. It thus follows that

$$\omega_J^+(x, x') = \sum_{p=0}^{\infty} \delta(2x_+ - x - x' + 2p(x_+ - x_-)) + \sum_{p=1}^{\infty} \delta(x - x' + 2p(x_+ - x_-)). \tag{52a}$$

A similar analysis for $\omega_J^-(x, x')$ shows that

$$\omega_J^-(x, x') = \sum_{p=0}^{\infty} \delta(2x_- - x - x' - 2p(x_+ - x_-)) + \sum_{p=1}^{\infty} \delta(x - x' - 2p(x_+ - x_-)). \tag{52b}$$

The solution $\omega_J(x, x')$ on $J \times J^c$ is found by combining the solutions on the subdomains $\omega_J^+(x, x')$ and $\omega_J^-(x, x')$

$$\omega_J(x, x') = \sum_{p \in \mathbb{Z}} \delta(2x_+ - x - x' + 2p(x_+ - x_-)) + \sum_{\substack{p \in \mathbb{Z}, \\ p \neq 0}} \delta(x - x' - 2p(x_+ - x_-)).$$

Assembling the temperature field $T_J(x, t)$ as in (27a) and (27d) now yields

$$T_J(x, t) = \sum_{p \in \mathbb{Z}} T_{J, \infty}(2x_+ - x + 2p(x_+ - x_-), t) + \sum_{p \in \mathbb{Z}} T_{J, \infty}(x + 2p(x_+ - x_-), t). \tag{54}$$

Similarly, the displacement potential $\psi_J(x, t)$ follows from (34a) and (34b)

$$\psi_J(x, t) = \sum_{p \in \mathbb{Z}} \psi_{J, \infty}(2x_+ - x + 2p(x_+ - x_-), t) + \sum_{p \in \mathbb{Z}} \psi_{J, \infty}(x + 2p(x_+ - x_-), t). \tag{55}$$

Taking the gradient and using (14) yields

$$u_J^{(T)}(x, t) = \sum_{p \in \mathbb{Z}} u_{J, \infty, x}(x + 2p(x_+ - x_-), t) - \sum_{p \in \mathbb{Z}} u_{J, \infty, x}(2x_+ - x + 2p(x_+ - x_-), t). \tag{56}$$

One can verify from this expression that $u_J(x_+, t) = 0$ and $u_J(x_-, t) = 0$, which is in agreement with (37).

Remark 10. Similar to the extensions of Example 1 in Examples 2 and 3, the results for the interval J extend to domains $J_n = \{\mathbf{x} \in \mathbb{R}^n \mid x_- < x_1 < x_+\}$.

Remark 11. The infinite sums that appear for example in (54) and (56) might seem cumbersome to compute. However, because the heat load $Q_{J, \infty}$ is only applied inside J (see (16)), the temperature fields $T_{J, \infty}(x, t)$ and displacement field $u_{J, \infty}(x, t)$ typically decay rapidly outside J and only a few terms with $|p|$ near 0 often gives accurate results.

Example 5 (The rectangle). Consider the rectangle $R = \{\mathbf{x} \in \mathbb{R}^2 \mid x_{-,1} < x_1 < x_{+,1}, x_{-,2} < x_2 < x_{+,2}\}$. This domain is not translation invariant in any direction, and the ultrahyperbolic Equations (28) for the kernel $\omega_R(\mathbf{x}, \mathbf{x}')$ can therefore not be reduced to a wave equation. However, based on some physical intuition and the formulas in [5], one can come up with the following formula

$$
\begin{aligned}
\omega_R(\mathbf{x}, \mathbf{x}') = &-\delta(x_1 - x_1')\delta(x_2 - x_2') \\
&+ \sum_{p, r \in \mathbb{Z}} (\delta(x_1 - x_1' + 2pL_1)\delta(x_2 - x_2' + 2rL_2) \\
&+ \delta(x_{I,1} - x' + 2pL_1)\delta(x_2 - x_2' + 2rL_2) \\
&+ \delta(x_1 - x_1' + 2pL_1)\delta(x_{I,2} - x_2' + 2rL_2) \\
&+ \delta(x_{I,1} - x_1' + 2pL_1)\delta(x_{I,2} - x_2' + 2rL_2)).
\end{aligned} \tag{57}
$$

where $L_1 = x_{+,1} - x_{-,1}, L_2 = x_{+,2} - x_{-,2}, x_{I,1} = 2x_{+,1} - x_1$, and $x_{I,2} = 2x_{+,2} - x_2$. One can verify that the kernel $\omega_R(\mathbf{x}, \mathbf{x}')$ in (57) indeed satisfies the conditions in (28). Using (27a) and (27d), the $T_R(\mathbf{x}, t)$ follows from (57) as

$$
\begin{aligned}
T_R(\mathbf{x}, t) = \sum_{p, r \in \mathbb{Z}} (&T_{R,\infty}(x_1 + 2pL_1, x_2 + 2rL_2, t) \\
&+ T_{R,\infty}(x_{I,1} + 2pL_1, x_2 + 2rL_2, t) \\
&+ T_{R,\infty}(x_1 + 2pL_1, x_{I,2} + 2rL_2, t) \\
&+ T_{R,\infty}(x_{I,1} + 2pL_1, x_{I,2} + 2rL_2, t)).
\end{aligned} \tag{58}
$$

Using (34a) and (34b), an expression for the displacement potential $\psi_R(\mathbf{x}, t)$ in terms of $\psi_{R,\infty}(\mathbf{x}, t)$ can be found. Taking the gradient of the expression for $\psi_R(\mathbf{x}, t)$ and using (14) yields

$$
\begin{aligned}
\begin{bmatrix} u_{R,1}^{(T)}(\mathbf{x}, t) \\ u_{R,1}^{(T)}(\mathbf{x}, t) \end{bmatrix} = \\
\sum_{p, r \in \mathbb{Z}} \Bigg(&\begin{bmatrix} u_{R,\infty,1}(x_1 + 2pL_1, x_2 + 2rL_2, t) \\ u_{R,\infty,2}(x_1 + 2pL_1, x_2 + 2rL_2, t) \end{bmatrix} \\
&+ \begin{bmatrix} -u_{R,\infty,1}(x_{I,1} + 2pL_1, x_2 + 2rL_2, t) \\ u_{R,\infty,2}(x_{I,1} + 2pL_1, x_2 + 2rL_2, t) \end{bmatrix} \\
&+ \begin{bmatrix} u_{R,\infty,1}(x_1 + 2pL_1, x_{I,2} + 2rL_2, t) \\ -u_{R,\infty,2}(x_1 + 2pL_1, x_{I,2} + 2rL_2, t) \end{bmatrix} \\
&- \begin{bmatrix} u_{R,\infty,1}(x_{I,1} + 2pL_1, x_{I,2} + 2rL_2, t) \\ u_{R,\infty,2}(x_{I,1} + 2pL_1, x_{I,2} + 2rL_2, t) \end{bmatrix} \Bigg).
\end{aligned} \tag{59}
$$

One can again verify that $\mathbf{u}_R^{(T)}(\mathbf{x}, t)$ satisfies (37b) and that $\sigma_{R,12}^{(T)} = 0$ on ∂R from this formula.

Remark 12. Similar ideas as in Example 5 can also be applied to the 3-D box $B = (x_{-,1}, x_{+,1}) \times (x_{-,2}, x_{+,2}) \times (x_{-,3}, x_{+,3})$, which is typically considered in welding applications, see for example [5]. The expressions for $\omega_B(\mathbf{x}, \mathbf{x}'), T_B(\mathbf{x}, t), \psi_B(\mathbf{x}, t)$, and $\mathbf{d}_B(\mathbf{x}, t)$ are similar to the ones for the rectangle R in Example 5, but now involve summations of $p, r, s \in \mathbb{Z}$ over all points in the set

$$
\{x_1 + 2pL_1, x_{I,1} + 2pL_1\} \times \{x_2 + 2rL_2, x_{I,2} + 2rL_2\} \times \{x_3 + 2sL_3, x_{I,3} + 2sL_3\}, \tag{60}
$$

where $\quad L_1 = x_{+,1} - x_{-,1}, L_2 = x_{+,2} - x_{-,2}, L_3 = x_{+,3} - x_{-,3}, x_{I,1} = 2x_{+,1} - x_1, x_{I,2} = 2x_{+,2} - x_2,$ and $x_{I,3} = 2x_{+,3} - x_3$.

Remark 13. The results in this section have been presented for zero Neumann BCs, but can be extended to zero Dirichlet BCs as well. However, this means that BCs for the kernels $\omega_\Omega(\mathbf{x}, \mathbf{x}')$ then also change from Neumann BCs such as (41c) to Dirichlet BCs. Because Dirichlet BCs lead to a change of sign when a wave is reflected at the boundary, expressions get sightly more involved. Some combinations of zero Dirichlet and Neumann BCs can be incorporated as well, see for example [5] where a box-shaped domain is considered with a zero Dirichlet BC at one side and zero Neumann BCs on all other sides.

Finally, it is demonstrated how the formula for the kernel on the half line with Robin BCs can be found from the conditions (28).

Example 6 (The half line with a Robin BC). Consider, just as in Example 1, the half line $HL = \{x \in \mathbb{R} \mid x < x_e\}$ but now with the Robin BC $aT_{HL} + \partial T_{HL}/\partial x = 0$ at $x = x_e$. As observed in Remark 7, the kernel $\omega_{HL}(x, x')$ should satisfy (28a), (28b), and (31b) for this BC. Similarly as in Example 1, (28a) implies that $\omega(x, x')$ is of the form (33a) and the ICs (28b) reduce (33a) to (33b), that is that

$$\omega_{HL}(x, x') = F_-(x + x' - 2x_e), \tag{61}$$

for a function $F_- : \mathbb{R} \to \mathbb{R}$. The ICs (28b) also imply that $F_-(\xi) = 0$ for $\xi < 0$. To determine $F_-(\xi)$ for $\xi \geq 0$, (61) is inserted in (31b)

$$aF_-(\xi) + \frac{\partial F_-}{\partial \xi}(\xi) = -a\delta(\xi) + \frac{\partial \delta}{\partial \xi}(\xi), \tag{62a}$$

where $\xi = x + x' - 2x_e$. To determine the solution of (62a), introduce $h(\xi) := F_-(\xi) - \delta(\xi)$ and note that

$$\frac{\partial h}{\partial \xi}(\xi) = \frac{\partial F_-}{\partial \xi}(\xi) - \frac{\partial \delta}{\partial \xi}(\xi) = -aF_-(\xi) - a\delta(\xi) = -ah(\xi) - 2a\delta(\xi), \tag{62b}$$

where the second identity follows from (62a) and the third from the definition of $h(\xi)$. Because $F(\xi) = h(\xi) = 0$ for $\xi < 0$, the solution of (62b) can be considered as the impulse response of a first-order system and is given by $h(\xi) = -2ae^{-a\xi}$ for $\xi > 0$. It thus follows that for $\xi \geq 0$

$$F_-(\xi) = \delta(\xi) - 2ae^{-a\xi}. \tag{62c}$$

Since $\xi = x + x' - 2x_e$, it follows that

$$\omega_{HL}(x, x') = \delta(x + x' - 2x_e) - 2ae^{-a(x+x'-2x_e)}, \tag{63}$$

for $x + x' - 2x_e \geq 0$ and that $\omega_{HL}(x, x') = 0$ otherwise. Inserting this expression into (27a) and (27d) yields

$$\tilde{T}_{HL}(x, t) = T_{HL,\infty}(2x_e - x, t) - 2a \int_{2x_e - x}^{\infty} e^{-a(x+x'-2x_e)} T_{HL,\infty}(x', t) dx'. \tag{64}$$

Formula (26) that is known from [1] can be recovered after applying the change of coordinates $x'' = x + x' - 2x_e$ in (64). Expressions for the displacement potential $\psi_{HL}(x, t)$ and displacement field $u_{HL}(x, t)$ can be obtained based on the expression for $\omega_{HL}(x, x')$ similarly as in Example 1.

4.2. The disk

For the spatial domains considered in the previous subsection, it was already known how the MoI should be applied to the temperature field but the kernel representation developed in Section 3 also enables the application of the MoI to domains to which it could not be applied before. This is illustrated by the results in this subsection, where the MoI is applied to the disk $D = \{\mathbf{x} \in \mathbb{R}^2 \mid x_1^2 + x_2^2 < R^2\}$. To the best of our knowledge, the MoI has not be applied to this domain before.

It will be more convenient to use the polar coordinates (r, θ) which are related to the Cartesian coordinates $\mathbf{x} = [x_1, x_2]^\top$ by

$$x_1 = r \cos(\theta), \qquad x_2 = r \sin(\theta). \tag{65a}$$

Furthermore, the radial and tangential components of the displacement field $\mathbf{u}_D(r, \theta, t)$ can be expressed in terms of the Cartesian components of $\mathbf{u}_D(\mathbf{x}, t)$ as

$$\begin{bmatrix} u_{D,r}(r, \theta, t) \\ u_{D,\theta}(r, \theta, t) \end{bmatrix} = \begin{bmatrix} \cos(\theta) & \sin(\theta) \\ -\sin(\theta) & \cos(\theta) \end{bmatrix} \begin{bmatrix} u_{D,1}(r \cos(\theta), r \sin(\theta), t) \\ u_{D,2}(r \cos(\theta), r \sin(\theta), t) \end{bmatrix} \tag{65b}$$

Because the disk $r < R$ is invariant under rotations, the kernel ω_D will only depend on $\hat{\theta} := \theta - \theta'$, r, and r', that is $\omega_D = \omega_D(r, \hat{\theta}, r')$. Expressing the gradient and Laplacian in polar coordinates, conditions (28) become

$$\frac{1}{r'} \frac{\partial}{\partial r'} \left(r' \frac{\partial \omega_D}{\partial r'} \right) + \frac{1}{r'^2} \frac{\partial^2 \omega_D}{\partial \hat{\theta}^2} = \frac{1}{r} \frac{\partial}{\partial r} \left(r \frac{\partial \omega_D}{\partial r} \right) + \frac{1}{r^2} \frac{\partial^2 \omega_D}{\partial \hat{\theta}^2}, \tag{66a}$$

$$\omega_D(r, \hat{\theta}, R) = \frac{\partial \omega_D}{\partial r'}(r, \hat{\theta}, R) = 0, \tag{66b}$$

$$\frac{\partial \omega_D}{\partial r}(R, \hat{\theta}, r') = \frac{1}{r'} \frac{\partial \delta}{\partial r'}(R - r')\delta(\hat{\theta}), \tag{66c}$$

where $\hat{\theta} = \theta - \theta' \in [-\pi, \pi), 0 \leq r < R$, and $r' > R$.

Remark 14. The factor $1/r'$ in (66c) appears because of the transformation to polar coordinates, see for example [26]. One can see that this factor is necessary because it now holds that for any test function $f = f(r, \theta)$

$$\int_0^\infty \int_0^{2\pi} f(r', \theta') \frac{1}{r'} \frac{\partial \delta}{\partial r'}(r - r')\delta(\theta - \theta') r' d\theta' dr'$$

$$= -\int_0^\infty \int_0^{2\pi} \frac{\partial f}{\partial r}(r', \theta')\delta(r - r')\delta(\theta - \theta') dr' d\theta' = -\frac{\partial f}{\partial r}(r, \theta). \tag{67}$$

Note that by interpreting $(r, \hat{\theta})$ as the 'spatial' coordinates and r' as the 'temporal' coordinate, (66) can be considered as a wave equation. By considering the weak form of (66), it is shown in Appendix B.2 that (66b) and (66c) imply that

$$\lim_{\varepsilon\downarrow 0}\omega_D(r,\hat{\theta},R+\varepsilon)=\frac{1}{R}\delta(r-R)\delta(\hat{\theta}),\tag{68a}$$

$$\lim_{\varepsilon\downarrow 0}\frac{\partial\omega_D}{\partial r'}(r,\hat{\theta},R+\varepsilon)=0,\tag{68b}$$

$$\frac{\partial\omega_D}{\partial r}(R,\hat{\theta},r')=0,\tag{68c}$$

for $r' > R$.

A closed-form analytic expression can now be obtained by writing the kernel $\omega_D(r,\hat{\theta},r')$ as a linear combination of the eigenfunctions of the Laplacian on the disk $(r,\hat{\theta})\in[0,R]\times[-\pi,\pi)$ satisfying zero Neumann BCs. To avoid very narrow features that are not clearly visible and to improve the convergence, the Dirac delta in the initial condition (68a) is replaced by the function $\delta_\gamma(r-R,\hat{\theta})$, where $\gamma > 0$ is a smoothing parameter. We choose $\delta_\gamma(r-R,\hat{\theta})$ equal to

$$\frac{1}{2\gamma^2R^2}\left(1+\cos\left(\frac{\pi(r-R)}{\gamma R}\right)\right)\left(1+\cos\left(\frac{\pi\hat{\theta}}{\gamma}\right)\right),\tag{69}$$

for $r\in[(1-\gamma)R,R]$ and $\hat{\theta}\in[-\gamma,\gamma]$ and zero otherwise. Note that $\delta_\gamma(r-R,\hat{\theta})$ approaches the Dirac in (68a) for $\gamma\to 0$. It is shown in Appendix C that the kernel $\omega_{D,\gamma}(r,\hat{\theta},r')$ satisfying (66a) and (68) with the Dirac in (68a) replaced by $\delta_\gamma(r-R,\hat{\theta})$ can be expressed as

$$\omega_{D,\gamma}(r,\hat{\theta},r')=\sum_{n=0}^{\infty}\sum_{m=1}^{\infty}A_{n,m}J_n\left(\beta_{n,m}\frac{r}{R}\right)\cos(n\hat{\theta})J_n\left(\beta_{n,m}\frac{r'}{R}\right),\tag{70a}$$

where J_n is the Bessel function of the first kind of order n, $\beta_{n,m}$ is the m-th root of $\partial J_n(r)/\partial r=0$, and $A_{n,m}$ are constants. The computation of the constants $A_{n,m}$ for $\gamma > 0$ is discussed in Appendix C. For $\gamma=0$, $A_{0,1}=1/(\pi R^2)$ and for all other values of n and m

$$A_{n,m}=\frac{1}{\pi R^2}\frac{2\beta_{n,m}^2}{\epsilon_n J_n^2(\beta_{n,m})\left(\beta_{n,m}^2-n^2\right)},\tag{70b}$$

where $\epsilon_n=2$ for $n=0$ and $\epsilon_n=1$ otherwise.

Remark 15. Note that

$$\omega_{D,\gamma}(r,\hat{\theta},r')=\frac{1}{R^2}\omega_{D,\gamma}^1\left(\frac{r}{R},\hat{\theta},\frac{r'}{R}\right),\tag{71}$$

where $\omega_{D,\gamma}^1(r,\hat{\theta},r')$ is the kernel for a disk of radius $R=1$, that is the shape of the kernel $\omega_{D,\gamma}(r,\hat{\theta},r')$ does not depend on the radius R.

The cross sections for r' and r constant in Figures 4 and 5 give an impression of the obtained kernel $\omega_{D,\gamma}(r,\hat{\theta},r')$. The axes in Figure 5 show $x_1'=r'\cos(\hat{\theta})$ and $x_2'=r'\sin(\hat{\theta})$. The parameter γ is set to $\gamma=0.05$ and the summation in (70a) is truncated to 31,250 terms ($n\in\{0,1,...,249\}$ and $m\in\{1,2,...,125\}$). The difference between this solution and the solution obtained with four times as many terms (i.e. $n\in\{0,1,...,499\}$ and $m\in\{1,2,...,250\}$) is less than 1% for all considered snapshots.

The cross sections of $\omega_{D,\gamma}(r,\hat{\theta},r')$ for r' constant in Figure 4 illustrate how the wave propagates inside the disk $(r,\hat{\theta})\in[0,R]\times[-\pi,\pi)$ as the 'time' r' increases. Observe that $\omega_{D,\gamma}(r,\hat{\theta},R)$ in Figure 4a is (an approximation of) a Dirac delta at $(r,\hat{\theta})=(R,0)$ at $r'=R$ and that the wave front in Figure 4b and c for $r' > R$ is not circular. The latter observation can be understood from the PDE (66a) which shows that the two terms involving $\partial^2\omega_D/\partial\hat{\theta}^2$ cancel each other for $r=R$
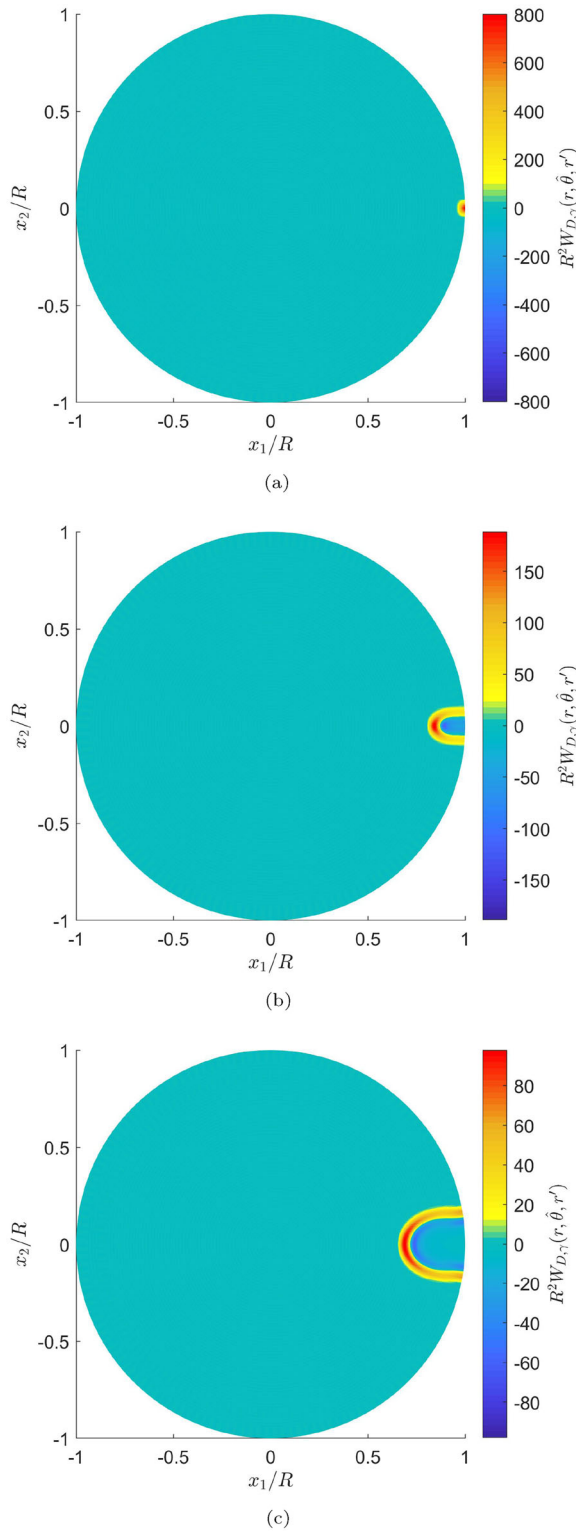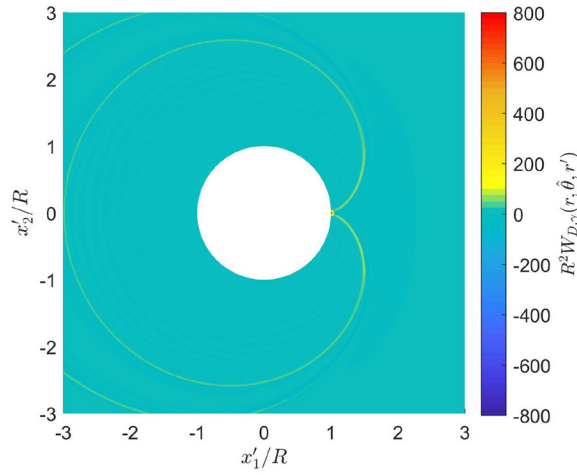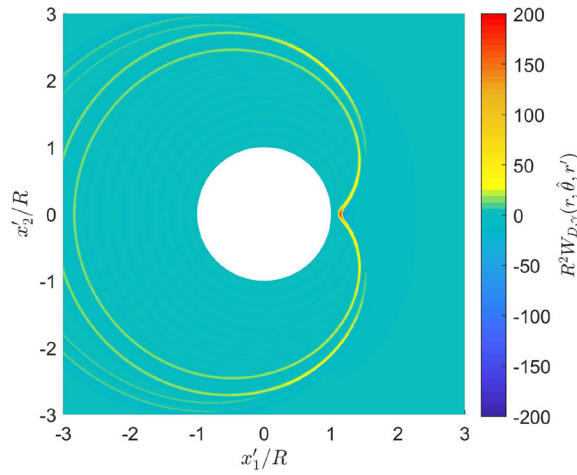
Figure 4. Cross sections of the kernel $\omega_{D,\gamma}(r, \hat{\theta}, r')$ for three different values of r' and $\gamma = 0.05$. (a) $r' = R$; (b) $r' = 1.15R$; (c) $r' = 1.3R$.
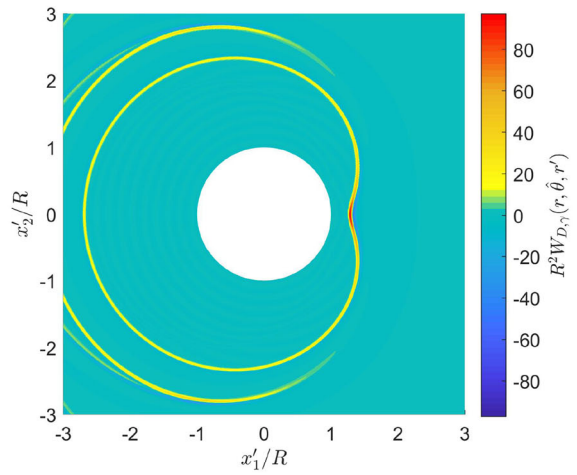
Figure 5. Cross sections of the kernel $\omega_{D,\gamma}(r, \hat{\theta}, r')$ for three different values of r and $\gamma = 0.05$.; (a) $r = R$; (b) $r = 0.85R$; (c) $r = 0.7R$.

and $r' = R$. At the initial 'time' $r' = R$, there is thus no diffusion in $\hat{\theta}$-direction and the wave propagates only in the r-direction. However, as $r' \to \infty$ the term involving $\partial^2 \omega_D / \partial \hat{\theta}^2$ on the LHS of (66a) vanishes and the propagation speed in the $\hat{\theta}$-direction increases.

The cross sections of $\omega_{D,\gamma}(r, \hat{\theta}, r')$ in Figure 5 are relevant for the computation of $\tilde{T}_D(r, \theta, t)$ according to (27d). A cross section $\omega_{D,\gamma}(r, \hat{\theta}, r') = \omega_{D,\gamma}(r, \theta - \theta', r')$ at $r = r_0$ shows the function that is multiplied with $T_{D,\infty}(r', \hat{\theta}, t) = T_{D,\infty}(r', \theta - \theta', t)$ and integrated over $(r', \theta') \in D^c = \mathbb{R}^2 \backslash D$ to obtain $\tilde{T}_D(r_0, \theta, t)$. Note that the cross section at $r = R$ in Figure 5a does not only show (an approximation of) a Dirac delta at $(r', \hat{\theta}) = (R, 0)$, but also shows two traces starting at $(r', \hat{\theta}) = (R, 0)$. These traces are no artifact of the truncation of the infinite sum in (70a), but indicate all 'time instances' r' at which a nonzero value occurs at $r = R$, that is all points at the boundary of cross sections for r' constant as the ones in Figure 4 where $\omega_{D,\gamma}$ is nonzero. The traces in Figure 5b and c have a similar interpretation, but they show the nonzero values of $\omega_{D,\gamma}$ at the circles $r = 0.9R$ and $r = 0.7R$, respectively.

The computation of $\tilde{T}_D(r, \theta, t)$ in (27d) is computationally expensive because the values of $\omega_{D,\gamma}(r, \theta - \theta', r')$ and $T_{D,\infty}(r', \theta', t)$ are needed in the whole domain $(r', \theta') \in D^c$ to compute $\tilde{T}_D(r, \theta, t)$ in one point (r, θ). Therefore, the kernel $\omega_D(r, \hat{\theta}, r')$ will be replaced by an approximation $\omega_{D,\text{appr}}(r, \hat{\theta}, r')$, which is obtained as follows. Because $T_{D,\infty}(r, \theta, t)$ will typically decrease rapidly outside D, it is most important that $\omega_{D,\text{appr}}(r, \hat{\theta}, r')$ is an accurate approximation of $\omega_D(r, \hat{\theta}, r')$ for r and r' near R. In this case, (66a) can be approximated by

$$\frac{\partial^2 \omega_{D,\text{appr}}}{\partial r'^2} + \frac{1}{R} \frac{\partial \omega_{D,\text{appr}}}{\partial r'} = \frac{\partial^2 \omega_{D,\text{appr}}}{\partial r^2} + \frac{1}{R} \frac{\partial \omega_{D,\text{appr}}}{\partial r}. \tag{72}$$

The solution of (72) with the ICs and the BC in (68) is

$$\omega_{D,\text{appr}}(r, \hat{\theta}, r') = \frac{1}{R} \delta((r - R) + (r' - R)) \delta(\hat{\theta}). \tag{73}$$

Inserting the kernel $\omega_{D,\text{appr}}(r, \hat{\theta}, r')$ into (27d) and again using the approximation $r' \approx R$ yields

$$\tilde{T}_{D,\text{appr}}(r, \theta, t) = \int_R^\infty \int_{-\pi}^\pi T_{D,\infty}(r', \theta', t) \omega_{D,\text{appr}}(r, \theta - \theta', r') R d\theta' dr' = T_{D,\infty}(2R - r, \theta, t), \tag{74}$$

so that (27a) shows that

$$T_{D,\text{appr}}(r, \theta, t) = T_{D,\infty}(r, \theta, t) + T_{D,\infty}(2R - r, \theta, t). \tag{75}$$

Note that the computation of $T_{D,\text{appr}}$ in a point (r, θ, t) only requires the evaluation of $T_{D,\infty}$ in two points and that $T_{D,\text{appr}}(r, \theta, t)$ is a good approximation of $T_D(r, \theta, t)$ near the edge $r = R$ because $\omega_{D,\text{appr}}(r, \theta, r')$ is a good approximation of $\omega_D(r, \theta, r')$ near $r' = R$.

The approximation of the displacement potential based on the approximation of the kernel in (73) can be obtained in a similar way as for $T_{D,\text{appr}}(r, \theta, t)$ as

$$\psi_{D,\text{appr}}(r, \theta, t) = \psi_{D,\infty}(r, \theta, t) + \psi_{D,\infty}(2R - r, \theta, t). \tag{76}$$

The displacement field $\mathbf{u}_D^{(T)}(r, \theta, t)$ can now be obtained by computing the gradient of (76). To this end, note that the gradient of $\psi_{D,\infty}(r, \theta, t)$ in polar coordinates is

$$\begin{bmatrix} u_{D,\infty,r}(\tilde{r}, \theta, t) \\ u_{D,\infty,\theta}(\tilde{r}, \theta, t) \end{bmatrix} = \begin{bmatrix} \dfrac{\partial \psi_{D,\infty}}{\partial r}(\tilde{r}, \theta, t) \\ \dfrac{1}{\tilde{r}} \dfrac{\partial \psi_{D,\infty}}{\partial \theta}(\tilde{r}, \theta, t) \end{bmatrix}, \tag{77}$$

Table 1. Considered parameter values.

Description	Symbol	Value	Unit
Wafer radius	R	150	mm
Wafer thickness	H	0.775	mm
Slit length in x_1	L_{slit}	26	mm
Slit length in x_2	W_{slit}	4.6	mm
Field length in x_1	L_{field}	26	mm
Field length in x_2	W_{field}	33	mm
Mass density	ρ	2329	kg/m^3
Specific heat capacity	c	705	J/kg/K
Thermal conductivity	k	149	W/m/K
Convection coefficient	h_0	1500	W/m^2/K
Young's modulus	E	167	GPa
Poisson's ratio	ν	0.3	–
Stiffness per unit area	k_0	1209	N/mm^3
Scan speed	v	0.276	m/s
Heating power	P_{EUV}	3.229	W

for all $(\tilde{r}, \theta) \in [0, \infty) \times [-\pi, \pi]$. Taking the gradient on both sides of (76) and using (14) thus shows that (for $(r, \theta) \in [0, R] \times [-\pi, \pi]$)

$$
\begin{bmatrix} u_{D,r}^{(T)}(r, \theta, t) \\ u_{D,\theta}^{(T)}(r, \theta, t) \end{bmatrix} = \begin{bmatrix} u_{D,\infty,r}(r, \theta, t) - u_{D,\infty,r}(2R - r, \theta, t) \\ u_{D,\infty,\theta}(r, \theta, t) + \dfrac{2R - r}{r} u_{D,\infty,\theta}(2R - r, \theta, t) \end{bmatrix}, \tag{78}
$$

where the second term on the RHS of the expression for $u_{D,\theta}^{(T)}(r, \hat{\theta}, t)$ can be understood by evaluating the second row in (77) in $(\tilde{r}, \theta, t) = (2R - r, \theta, t)$ which shows that

$$
\frac{\partial \psi_{D,\infty}}{\partial \theta}(2R - r, \theta, t) = (2R - r)u_{D,\infty,\theta}(2R - r, \theta, t). \tag{79}
$$

Formulas (75) and (78) will be applied to the wafer heating application in the next section.

5. Wafer heating

In this section, a part of the theory developed in the previous sections will be applied to a wafer heating problem. In this application, a thin silicon disk, called the wafer, is exposed to a light source which creates a pattern of electronic connections (see Figure 1). Because the wafer is thin, a 2-D plane-stress model is used, just as in [11, 19]. The temperature field $T_D(\mathbf{x}, t)$ and the displacement field $\mathbf{u}_D(\mathbf{x}, t)$ resulting from the heat load $Q_D(\mathbf{x}, t)$ are thus solutions of (1) with BCs (6), where $D = \{\mathbf{x} \in \mathbb{R}^2 \mid x_1^2 + x_2^2 < R^2\}$ and the coefficients in (1) are given by (3a) and (3b). The used parameter values in Table 1 are based on a representative case study also considered in [11]. The accurate and efficient computation of the resulting temperature and displacement fields $T_D(\mathbf{x}, t)$ and $\mathbf{u}_D(\mathbf{x}, t)$ is important, because such predictions can be used to assess and subsequently improve the quality of the lithography process.

The pattern of electronic connections is not projected to the whole wafer at once, but only in a small rectangular area $\Omega_{\text{slit}}(t)$, called the slit, which moves over the wafer surface, see Figure 1. The heat load $Q_D(\mathbf{x}, t)$ induced by the projection light is modeled as a uniform heat load in $\Omega_{\text{slit}}(t)$ with a constant intensity P_{EUV}. The exposure of the wafer is illustrated in Figure 1, which shows how the slit consecutively scans all fields on the wafer (light blue rectangles). Typically, the same pattern of electronic connections is projected in each field on the wafer. During the scanning of each field the heat load moves with a constant velocity v. The relevant dimensions of the
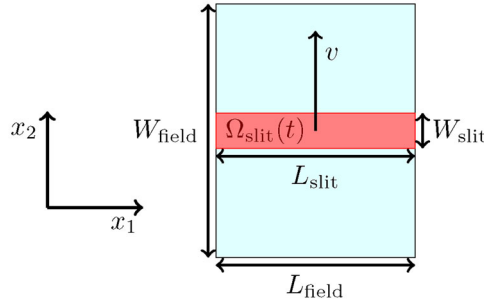
Figure 6. Dimensions of one field (light blue) and of the slit (red).

slit and of a field are illustrated in Figure 6. Note that fields in Figure 1 are scanned alternately in the positive and negative x_2-direction. Also note that because the pattern of electronic connections is projected only inside $\Omega_{\text{slit}}(t)$, the displacement field $\mathbf{u}_D(\mathbf{x}, t)$ inside $\Omega_{\text{slit}}(t)$ will determine the imaging quality of the lithography process.

It is assumed that after the scanning of one field is completed, the heat load instantly moves to the next field, but if desired some time delay needed to switch to the next field could have been taken into account as well. Note that the heat load applied to each field is the same, only the location, the scanning direction, and the time at which the slit arrives varies for the different fields. This means that (the extension to $\mathbb{R}^2$ of) the applied heat load $Q_{D,\infty}(\mathbf{x}, t)$ can be written in the form (17). When $Q_{\text{pass}}(\mathbf{x}, t)$ is the heat load applied to a single field centered at $\mathbf{x} = \mathbf{0}$ that is scanned in the positive x_2-direction starting at time $t = 0$, the i-th shift in space $\mathbf{x}_i$ is the center of the i-th field, the i-th rotation matrix $\mathbf{R}_i = \mathbf{I}$ when the i-th field is scanned in the positive x_2-direction and $\mathbf{R}_i = -\mathbf{I}$ when the i-th field is scanned in the negative x_2-direction, and the i-th shift in time τ_i is the time at which the scanning of the i-th field starts. On $\mathbb{R}^2$, the temperature and displacement fields $T_{D,\infty}(\mathbf{x}, t)$ and $\mathbf{u}_{D,\infty}(\mathbf{x}, t)$ resulting from the repetitive heat load $Q_{D,\infty}(\mathbf{x}, t)$ can thus be constructed from the responses $T_{\text{pass}}(\mathbf{x}, t)$ and $\mathbf{u}_{\text{pass}}(\mathbf{x}, t)$ resulting from $Q_{\text{pass}}(\mathbf{x}, t)$ according to (19) and (22), respectively.

Note that solutions can also be considered as a function of the polar coordinates (r, θ), for example $T_{D,\infty}(\mathbf{x}, t)$ can also be considered as $T_{D,\infty}(r, \theta, t)$. Based on the approximation of the true kernel $\omega_D(r, \theta - \theta', t)$ in (70) by $\omega_{D,\text{appr}}(r, \theta - \theta', r')$ in (73), the true solutions $T_D(r, \theta, t)$ and $\mathbf{u}_D(r, \theta, t)$ can be approximated by $T_{D,\text{appr}}(r, \theta, t)$ and $\mathbf{u}_{D,\text{appr}}(r, \theta, t)$ in (75) and (78), respectively.
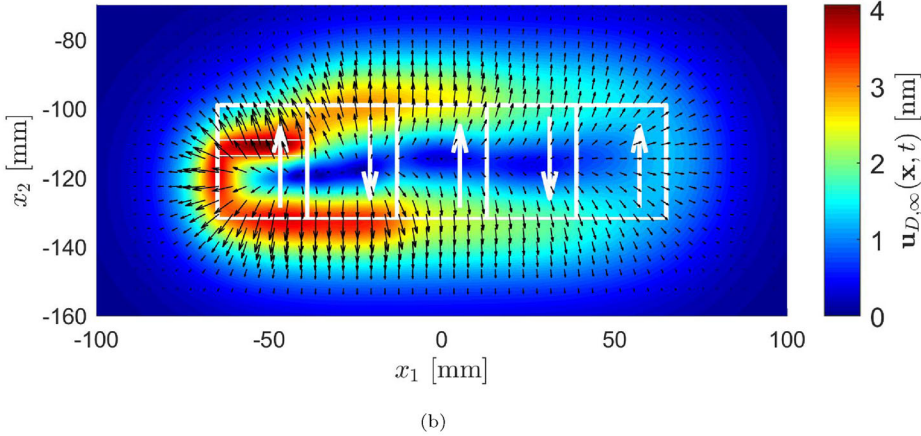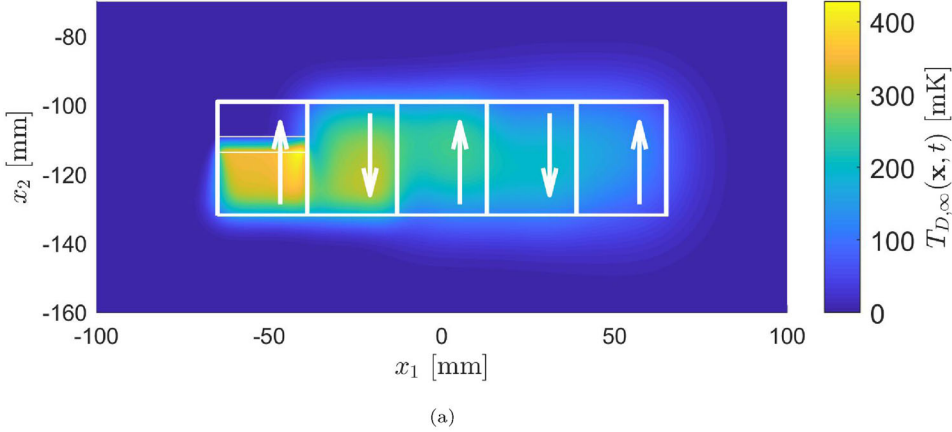
First, the construction of the temperature and displacement fields at one particular time instant (and for all $\mathbf{x} \in D$) using the MoI will be demonstrated in Subsection 5.1 because this illustrates the proposed method clearly. Subsequently, a more practical case will be considered in Subsection 5.2 where the MoI is used to compute overlay maps. These show the deformation that is observed at each point in the wafer surface at the moment it is scanned and thus provide the information that is relevant for the quality of the lithography process.

5.1. Snapshots at a particular time instant

First, the construction of the temperature and displacement fields at a particular time instant $t_1 = 0.628$ s will be considered. At this time instant, the fifth field in the expose pattern in Figure 1 is being scanned. The solutions $T_{D,\text{appr}}(\mathbf{x}, t_1)$ and $\mathbf{u}_{D,\text{appr}}(\mathbf{x}, t_1)$ obtained using the MoI with the kernel in (73) will be compared to the solutions $T_D(\mathbf{x}, t_1)$ and $\mathbf{u}_D(\mathbf{x}, t_1)$ obtained through the used standard FE analysis. Recall that the repetitive nature of the applied heat load is exploited in the construction of $T_{D,\text{appr}}(\mathbf{x}, t_1)$ and $\mathbf{u}_{D,\text{appr}}(\mathbf{x}, t_1)$ based on the responses $T_{\text{pass}}(\mathbf{x}, t)$ and $\mathbf{u}_{\text{pass}}(\mathbf{x}, t)$,

Table 2. The number of spatial and temporal grid points used to compute the snapshots $T_D(\mathbf{x}, t_1), \mathbf{u}_D(\mathbf{x}, t_1), T_{D, \text{appr}}(\mathbf{x}, t_1)$, and $\mathbf{u}_{D, \text{appr}}(\mathbf{x}, t_1)$ for $t = t_1 = 0.628$ s.

| L_e [mm]	# spatial grid points			# temporal grid points	
	$T_D(\mathbf{x}, t), T_{D, \text{appr}}(\mathbf{x}, t)$ $\mathbf{u}_D(\mathbf{x}, t), \mathbf{u}_{D, \text{appr}}(\mathbf{x}, t)$	$T_{\text{pass}}(\mathbf{x}, t)$ $\mathbf{u}_{\text{pass}}(\mathbf{x}, t)$	$\mathbf{u}_D^{(BC)}(\mathbf{x}, t)$	$T_D(\mathbf{x}, t), T_{D, \text{appr}}(\mathbf{x}, t)$ $\mathbf{u}_D(\mathbf{x}, t), \mathbf{u}_{D, \text{appr}}(\mathbf{x}, t)$	$T_{\text{pass}}(\mathbf{x}, t)$ $\mathbf{u}_{\text{pass}}(\mathbf{x}, t)$
2	3,782	2,132	793	158	68
1	15,030	8,343	3,146	315	135
1/2	59,914	33,005	12,291	629	269
1/4	239,290	131,289	48,581	1,257	537
1/8	956,346	523,697	193,161	2,513	1,073
1/16	3,823,838	—	—	5,025	—

(a)

(b)

Figure 7. The temperature field $T_{D, \infty}(\mathbf{x}, t_1)$ and the displacement field $\mathbf{u}_{D, \infty}(\mathbf{x}, t_1)$ on $\mathbb{R}^2$ constructed from $T_{\text{pass}}(\mathbf{x}, t)$ and $\mathbf{u}_{\text{pass}}(\mathbf{x}, t)$. The white rectangles with arrows indicate the considered fields with their scanning directions. (a) $T_{D, \infty}(\mathbf{x}, t)$; (b) $\mathbf{u}_{D, \infty}(\mathbf{x}, t)$.
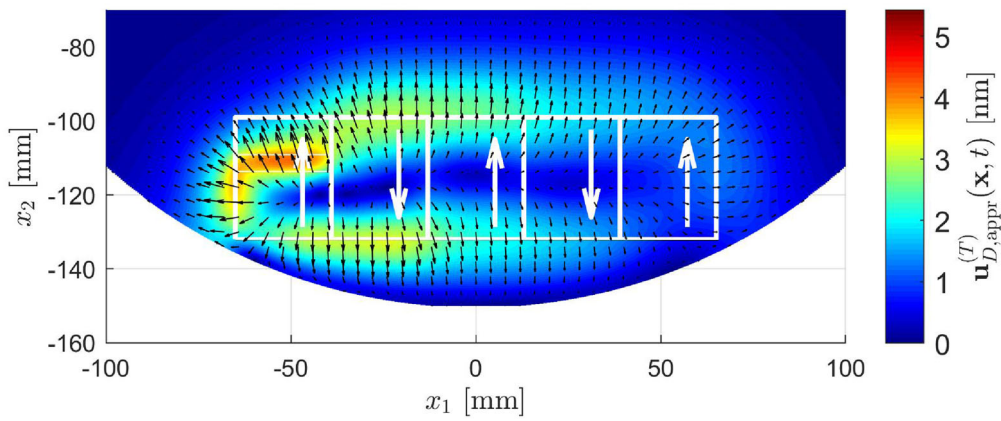
but that such an approach is not possible in the computation of $T_D(\mathbf{x}, t_1)$ and $\mathbf{u}_D(\mathbf{x}, t_1)$ by the used standard FE method.

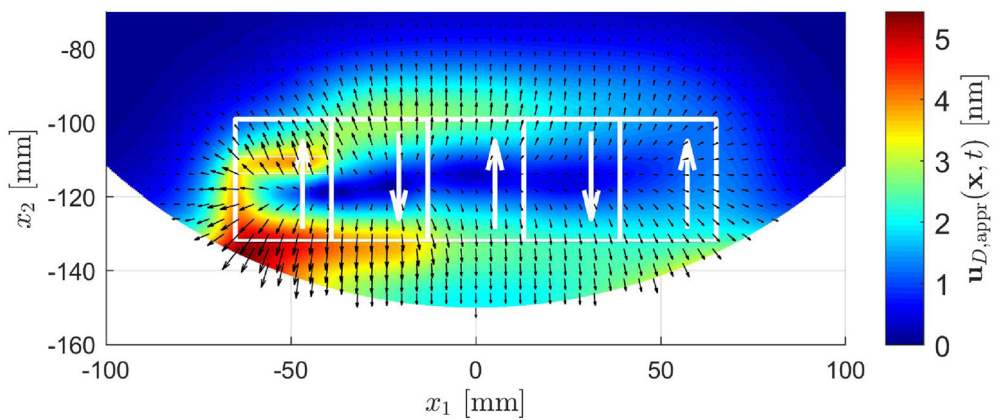### 5.1.1. Spatial and temporal discretization

The standard FE solutions $T_D(\mathbf{x}, t_1)$ and $\mathbf{u}_D(\mathbf{x}, t_1)$ will be computed based on several spatial and temporal grids, which are characterized by L_e, the smallest element size in the spatial grid. The
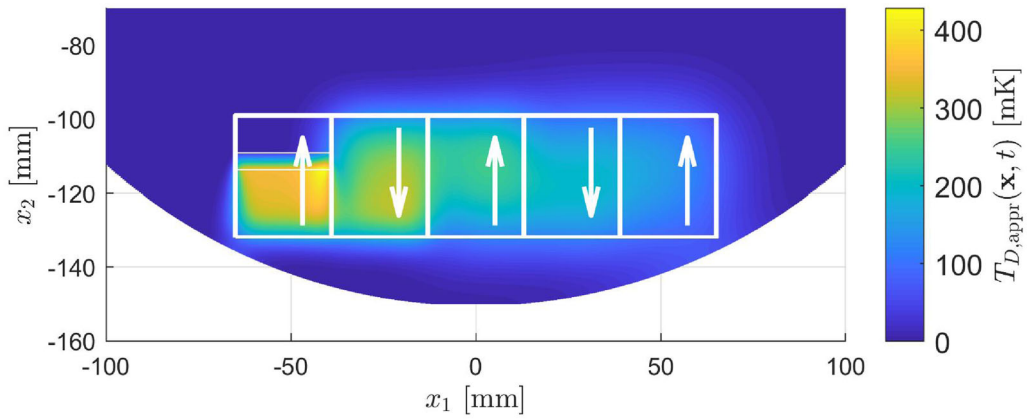
(a)

(b)

(c)

Figure 8. The temperature field $T_{D,\text{appr}}(\mathbf{x}, t_1)$ (a) and the displacement fields $\mathbf{u}_{D,\text{appr}}^{(T)}(\mathbf{x}, t_1)$ (b) and $\mathbf{u}_{D,\text{appr}}(\mathbf{x}, t_1) = \mathbf{u}_{D,\text{appr}}^{(T)}(\mathbf{x}, t_1) + \mathbf{u}_{D,\text{appr}}^{(BC)}(\mathbf{x}, t_1)$ (c) at $t_1 = 0.628$ s. The white rectangles with arrows indicate the considered fields with their scanning directions.

Table 3. Computational times for the snapshots $T_D(\mathbf{x}, t_1)$ and $\mathbf{u}_D(\mathbf{x}, t_1)$ by the used standard FE approach at $t_1 = 0.628$ s.

L_e [mm]	T_D	$\mathbf{u}_D$	total
2	0.4 s	<0.1 s	1.4 s
1	3.6 s	0.2 s	5.2 s
1/2	27.4 s	0.8 s	33.8 s
1/4	260.0 s	4.7 s	287.0 s
1/8	2228.3 s	99.6 s	2424.0 s
1/16*	20015.3 s	379.4 s	20763.9 s

Table 4. Computational times for the snapshots $T_{D,\,\mathrm{appr}}(\mathbf{x}, t_1)$ and $\mathbf{u}_{D,\,\mathrm{appr}}(\mathbf{x}, t_1)$ using the MoI at $t_1 = 0.628$ s.

L_e [mm]	T_{pass} & $\mathbf{u}_{\mathrm{pass}}$	$\mathbf{u}_{D,\,\mathrm{appr}}^{(BC)}$	total
2	0.4 s	0.5 s	1.1 s
1	1.5 s	1.2 s	3.3 s
1/2	9.6 s	4.3 s	15.9 s
1/4	68.0 s	17.3 s	93.5 s
1/8	516.2 s	71.9 s	620.6 s

Table 5. Absolute (and relative) errors in the solutions $T_{D,\,\mathrm{appr}}(\mathbf{x}, t_1)$ computed using the MoI and the solutions $T_D(\mathbf{x}, t_1)$ computed by the used standard FE method for $t_1 = 0.628$ s.

L_e [mm]	MoI		FE	
2	18.4 mK	(4.3%)	51.3 mK	(12.0%)
1	10.2 mK	(2.4%)	17.1 mK	(4.0%)
1/2	2.4 mK	(0.6%)	9.9 mK	(2.3%)
1/4	1.6 mK	(0.4%)	3.7 mK	(0.9%)
1/8	1.6 mK	(0.4%)	1.3 mK	(0.3%)

Table 6. Absolute (and relative) errors in the solutions $\mathbf{u}_{D,\,\mathrm{appr}}(\mathbf{x}, t_1)$ computed using the MoI and the solutions $\mathbf{u}_D(\mathbf{x}, t_1)$ computed by the used standard FE method for $t_1 = 0.628$ s.

L_e [mm]	MoI		FE	
2	0.27 nm	(5.1%)	1.32 nm	(25.0%)
1	0.20 nm	(3.9%)	0.53 nm	(10.0%)
1/2	0.18 nm	(3.4%)	0.30 nm	(6.8%)
1/4	0.19 nm	(3.4%)	0.12 nm	(2.3%)
1/8	0.18 nm	(3.4%)	0.05 nm	(0.9%)

spatial grid used for the FE solutions is based on a rectangular grid that covers the area $(x_1, x_2) \in [-194, 194] \times [-150, -38]$ mm^2, but elements that fall (partially) outside the disk D are discarded. The element size in the x_1-direction is L_e when $x_1 \in [-90, 90]$ mm and $4L_e$ otherwise. The element size in the x_2-direction is L_e when $x_2 \in [-150, -70]$ and $4L_e$ otherwise. The element size is increased near the edges of the considered domain because $T_D(\mathbf{x}, t_1)$ and $\mathbf{u}_D(\mathbf{x}, t_1)$ are small in these areas. The time interval $I = [0, t_1]$ is discretized with a uniform time step of L_e/v_e, where $v_e = 0.5$ m/s. Note that $v_e > v$, which assures that the heat load does not move over more than one element in each time step. The number of points in these spatial and temporal grids are given in Table 2.

The solutions $T_{D,\,\mathrm{appr}}(\mathbf{x}, t_1)$ and $\mathbf{u}_{D,\,\mathrm{appr}}(\mathbf{x}, t_1)$ obtained by the MoI are evaluated on the same spatial grid as the standard FE solutions. The computation of $T_{D,\,\mathrm{appr}}(\mathbf{x}, t_1)$ and $\mathbf{u}_{D,\,\mathrm{appr}}(\mathbf{x}, t_1)$ also requires the computation of the single-field solutions $T_{\mathrm{pass}}(\mathbf{x}, t)$ and $\mathbf{u}_{\mathrm{pass}}(\mathbf{x}, t)$. The spatial grid used for the computation of $T_{\mathrm{pass}}(\mathbf{x}, t)$ and $\mathbf{u}_{\mathrm{pass}}(\mathbf{x}, t)$ covers the area $(x_1, x_2) \in [-82, 82] \times [-105, 105]$ mm^2. The element size in the x_1-direction is L_e when $x_1 \in [-26, 26]$ mm and $4L_e$ otherwise and the element size in x_2-direction is L_e when $x_2 \in [-33, 33]$ and $4L_e$ otherwise. The

Table 7. Computational times for the overlay maps $e_{\text{appr}}(\mathbf{x})$ and MA deformation $\mathbf{u}_{e,\text{appr}}(\mathbf{x})$ computed using the MoI and for the overlay maps $e(\mathbf{x})$ and MA deformation $\mathbf{u}_e(\mathbf{x})$ computed by the used standard FE method for $t \in [0, t_1]$ with $t_1 = 0.628$ s.

L_e [mm]	$\mathbf{u}_{\text{pass}}$	MoI	FE
2	0.6 s	1.5 s	2.8 s
1	5.2 s	7.6 s	20.0 s
1/2	56.1 s	69.4 s	162.4 s
1/4	680.0 s	779.6 s	1485.8 s
1/8*	—	—	12498.6 s

Table 8. Absolute (and relative) errors in the overlay maps $e_{\text{appr}}(\mathbf{x})$ computed using the MoI and in the overlay maps $e(\mathbf{x})$ computed by the used standard FE method for $t \in [0, t_1]$ with $t_1 = 0.628$ s.

L_e [mm]	MoI		FE	
2	0.27 nm	(5.5%)	0.39 nm	(7.9%)
1	0.12 nm	(2.4%)	0.12 nm	(2.5%)
1/2	0.07 nm	(1.5%)	0.06 nm	(1.2%)
1/4	0.07 nm	(1.4%)	0.02 nm	(0.5%)

temporal grid uses a time step of L_e/v_e on the interval $t \in [0, 0.148]$ during which the heat load is applied and a time step of $4L_e/v_e$ on the interval $t \in [0.148, t_1]$ during which the applied heat load is zero. The computation of $\mathbf{u}_{D,\text{appr}}(\mathbf{x}, t_1)$ also requires the computation of the edge correction $\mathbf{u}_{D,\text{appr}}^{(BC)}(\mathbf{x}, t_1)$ at the final time instant $t = t_1$. This solution is computed in polar coordinates on a grid that covers the area $(r, \theta) \in [98, 150]$mm $\times [-\pi/2 - 0.8, -\pi/2 + 0.8]$ rad. The element size is $2L_e$ in the r-direction and the elements cover an angle $2L_e/R$ in the θ-direction. The number of points in these spatial and temporal grids are given in Table 2.

The construction of the FE matrices required for the computation of $T_D(\mathbf{x}, t), \mathbf{u}_D(\mathbf{x}, t), T_{\text{pass}}(\mathbf{x}, t), \mathbf{u}_{\text{pass}}(\mathbf{x}, t)$, and $\mathbf{u}_{D,\text{appr}}^{(BC)}(\mathbf{x}, t)$ is implemented in MATLAB (R2019a) and is based on FE tooling developed at ASML, which was also used in [27]. Linear Lagrangian shape functions are used, which means that the number of spatial grid points in Table 2 is equal to the number of nodes in the FE model. The time integration is done using the Crank-Nicolson scheme [28]. Lower-Upper (LU) matrix decompositions are used for the linear systems that need to be solved at every time step.

5.2. Graphical illustration

The first step to obtain $T_{D,\text{appr}}(\mathbf{x}, t)$ and $\mathbf{u}_{D,\text{appr}}(\mathbf{x}, t)$ using the MoI is the construction of the temperature and displacement fields $T_{D,\infty}(\mathbf{x}, t)$ and $\mathbf{u}_{D,\infty}(\mathbf{x}, t)$ on $\mathbb{R}^2$ based on the single-field responses $T_{\text{pass}}(\mathbf{x}, t)$ and $\mathbf{u}_{\text{pass}}(\mathbf{x}, t)$ according to (19) and (22). This requires the interpolation of $T_{\text{pass}}(\mathbf{x}, t)$ and $\mathbf{u}_{\text{pass}}(\mathbf{x}, t)$, which is done using MATLAB's `griddedInterpolant` function. The snapshots $T_{D,\infty}(\mathbf{x}, t_1)$ and $\mathbf{u}_{D,\infty}(\mathbf{x}, t_1)$ at $t_1 = 0.628$ s are shown in Figure 7.

Based on $T_{D,\infty}(\mathbf{x}, t_1)$ and $\mathbf{u}_{D,\infty}(\mathbf{x}, t_1)$ in Figure 7, the approximations $T_{D,\text{appr}}(r, \theta, t_1)$ and $\mathbf{u}_{D,\text{appr}}^{(T)}(r, \theta, t_1)$ can then be computed according to (75) and (78) and are shown in Figure 8a and b, respectively. Note that (75) and (78) are formulated in polar coordinates but that $T_{D,\infty}(\mathbf{x}, t_1)$ and $\mathbf{u}_{D,\infty}(\mathbf{x}, t_1)$ are computed in Cartesian coordinates. This step thus requires a conversion from Cartesian to polar coordinates according to (65). As the reflections along radial lines in (75) and (78) are not compatible with the used rectangular grids, this step also requires the interpolation of $T_{D,\infty}(\mathbf{x}, t)$ and $\mathbf{u}_{D,\infty}(\mathbf{x}, t)$ which is again implemented using MATLAB's gridded Interpolant function.

The displacement field $\mathbf{u}_{D,\text{appr}}^{(T)}(r, \theta, t_1)$ that satisfies the stress free BCs (6b) still requires the computation of the edge correction $\mathbf{u}_{D,\text{appr}}^{(BC)}(r, \theta, t)$, which is the solution of (11) with BC (12). Note that $T_{D,\infty}(r, \theta, t)$ and $\mathbf{u}_{D,\infty}(r, \theta, t)$ appear in (12) through $\boldsymbol{\sigma}^{(T)}(\mathbf{x}, t)$. The found displacement

field $\mathbf{u}_{D, \text{appr}}(r, \theta, t_1) = \mathbf{u}_{D, \text{appr}}^{(T)}(r, \theta, t_1) + \mathbf{u}_{D, \text{appr}}^{(BC)}(r, \theta, t_1)$ is shown in Figure 8c, which shows that the edge correction $\mathbf{u}_{D, \text{appr}}^{(BC)}(r, \theta, t)$ is significant. Note that $T_{D, \text{appr}}(\mathbf{x}, t_1)$ and $\mathbf{u}_{D, \text{appr}}(\mathbf{x}, t_1)$ can be obtained by inverting (65).

5.3. Computational times & accuracy

Most simulations in this section have been done on a laptop with 8 GB RAM, but some simulations on very fine grids require more memory and have been done on a desktop with 32 GB RAM. The latter results are indicated by a *.

Table 3 shows the computational times required to obtain $T_D(\mathbf{x}, t_1)$ and $\mathbf{u}_D(\mathbf{x}, t_1)$ using the used standard FE method. Note that the computation of $T_D(\mathbf{x}, t)$ is more time consuming than the computation of the resulting displacement field $\mathbf{u}_D(\mathbf{x}, t_1)$ because $T_D(\mathbf{x}, t)$ is computed at all considered time instances, whereas $\mathbf{u}_D(\mathbf{x}, t_1)$ is computed only at the final time instant $t = t_1 = 0.628$ s.

Table 4 shows the computational times required to obtain $T_{D, \text{appr}}(\mathbf{x}, t_1)$ and $\mathbf{u}_{D, \text{appr}}(\mathbf{x}, t_1)$ using the MoI. The most time-consuming steps are the computation of the responses $T_{\text{pass}}(\mathbf{x}, t)$ and $\mathbf{u}_{\text{pass}}(\mathbf{x}, t)$ for one field and the computation of $\mathbf{u}^{(BC)}(\mathbf{x}, t_1)$. These are indicated separately. Comparing the total times in Tables 3 and 4 shows that, on finer grids, the times for the MoI are clearly becoming shorter than the times for the used standard FE method. Note that the total times in Tables 3 and 4 also include overheads such as the construction of the FE matrices and thus exceed the sum of the times in the other two columns.

Using the standard FE solution on the $L_e = 1/16$ mm grid as a reference, the error in $T_{D, \text{appr}}(\mathbf{x}, t_1)$ and $\mathbf{u}_{D, \text{appr}}(\mathbf{x}, t_1)$ obtained using the MoI can be compared to the error in $T_D(\mathbf{x}, t)$ and $\mathbf{u}_D(\mathbf{x}, t)$ obtained by the used standard FE method. The resulting temperature and displacement errors (measured in the sup-norm) are given in Tables 5 and 6, respectively. It is worth noting that the maximal error in the FE solutions $T_D(\mathbf{x}, t_1)$ and $\mathbf{u}_D(\mathbf{x}, t_1)$ occurs on the edge of the wafer (around the point $(x_1, x_2) = (-65, -135)$ mm for $T_D(\mathbf{x}, t_1)$ and near the point $(x_1, x_2) = (-68, -134)$ mm for $\mathbf{u}_D(\mathbf{x}, t_1)$). This seems to indicate that the errors in the FE solutions are mostly due to the approximation of the circular edge by rectangular elements. On the $L_e = 1/4$ mm and $L_e = 1/8$ mm grids, the maximal error in $T_{D, \text{appr}}(\mathbf{x}, t_1)$ occurs on the edge around the point $(x_1, x_2) = (-59, -138)$ mm. On the coarser grids, the maximal error in $T_{D, \text{appr}}(\mathbf{x}, t_1)$ occurs inside $\Omega_{\text{slit}}(t_1)$ where the temperature gradient is the steepest. The maximal error in $\mathbf{u}_{D, \text{appr}}(\mathbf{x}, t_1)$ occurs on the edge around the point $(x_1, x_2) = (-56, -139)$ mm for all considered grids.

It is remarkable to see that the solutions computed using the MoI are often more accurate than the solutions computed using the used standard FE method, especially on the coarser grids. Note that the error in $T_{D, \text{appr}}(\mathbf{x}, t_1)$ stops decreasing at the $L_e = 1/4$ mm grid and that the error in $\mathbf{d}_D(\mathbf{x}, t_1)$ stops decreasing at the $L_e = 1/2$ mm grid. This indicates that the errors in $T_{D, \text{appr}}(\mathbf{x}, t_1)$ and $\mathbf{u}_{D, \text{appr}}(\mathbf{x}, t_1)$ introduced by the approximation of $\omega_D(r, \hat{\theta}, r')$ in (70a) by $\omega_{D, \text{appr}}(r, \hat{\theta}, r')$ in (73) are for the considered simulation approximately 1.6 mK and 0.18 nm, respectively.

Note that the error in the FE solutions $T_D(\mathbf{x}, t_1)$ and $\mathbf{u}_D(\mathbf{x}, t_1)$ in Tables 5 and 6 is approximately halved each time the element size L_e is halved. Extrapolating this trend to the $L_e = 1/16$ mm grid, the estimated error in $T_D(\mathbf{x}, t_1)$ is still of a similar magnitude as the error in $T_{D, \text{appr}}(\mathbf{x}, t_1)$ on the $L_e = 1/8$ mm grid. On the $L_e = 1/4$ mm and $L_e = 1/8$ mm grids, the maximal errors in the FE solutions $T_D(\mathbf{x}, t_1)$ also occur at locations that are close to the locations where the maximal error in the MoI solutions $T_{D, \text{appr}}(\mathbf{x}, t_1)$ occur. It is therefore possible that the estimated error in $T_{D, \text{appr}}(\mathbf{x}, t_1)$ of 1.6 mK is still influenced by the accuracy of the used reference solution. We were not able to compute a reference solution on grids finer than the $L_e = 1/16$
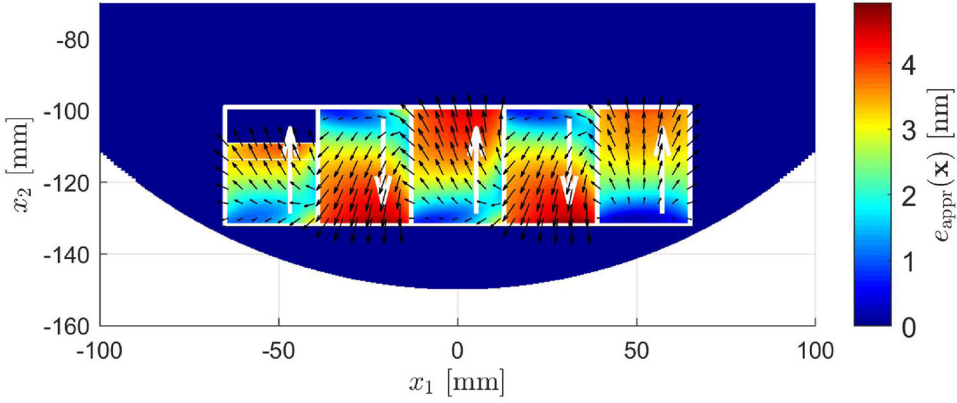
Figure 9. Overlay map for $t \in [0, t_1]$ with $t_1 = 0.628$ s computed using the MoI on the $L_e = 1/4$ mm grid. The color scale and the black arrows indicate $e_{\mathrm{appr}}(\mathbf{x})$ and $\mathbf{u}_{e,\mathrm{appr}}(\mathbf{x})$, respectively. The white rectangles with arrows indicate the considered fields with their scanning directions.

mm grid due to the high computational times, see Table 3, and the increasing memory requirements. However, the results clearly demonstrate that, for the considered wafer heating problem, the accuracy of the proposed method is comparable to the accuracy of a standard FE model that can be solved in a reasonable amount of time. Note that the error in the reference solution will only have a minor influence on the estimated error of 0.18 nm in $\mathbf{u}_{D,\mathrm{appr}}(\mathbf{x}, t_1)$.

5.4. Overlay maps

The construction of the snapshots in the previous subsection was mainly used to illustrate the proposed method. In this subsection, the construction of overlay maps using the MoI will be demonstrated. These overlay maps show the moving-average (MA) overlay $e(\mathbf{x})$ defined as

$$e(\mathbf{x}) = \frac{1}{t_+(\mathbf{x}) - t_-(\mathbf{x})} \int_{t_-(\mathbf{x})}^{t_+(\mathbf{x})} \|\mathbf{u}_D(\mathbf{x}, t)\| \mathrm{d}t, \qquad (80\mathrm{a})$$

where $t_-(\mathbf{x})$ and $t_+(\mathbf{x})$ denote the starting point and end point of the time interval during which the point $\mathbf{x}$ is exposed to the projection light, that is $Q_D(\mathbf{x}, t)$ is nonzero precisely for $t \in [t_-(\mathbf{x}), t_+(\mathbf{x})]$. For points $\mathbf{x}$ that are never exposed to the projection light, $e(\mathbf{x})$ is set to zero. The MA overlay $e(\mathbf{x})$ thus gives a good indication of the degradation in imaging quality due to wafer heating. To get some indication of the occurring deformation, the figures in this subsection will also display

$$\mathbf{u}_e(\mathbf{x}) = \frac{1}{t_+(\mathbf{x}) - t_-(\mathbf{x})} \int_{t_-(\mathbf{x})}^{t_+(\mathbf{x})} \mathbf{u}_D(\mathbf{x}, t) \mathrm{d}t. \qquad (80\mathrm{b})$$

Note that the norm of $\mathbf{u}_e(\mathbf{x})$ is not equal to $e(\mathbf{x})$. The MA overlay $e_{\mathrm{appr}}(\mathbf{x})$ and the MA deformation $\mathbf{u}_{e,\mathrm{appr}}(\mathbf{x})$ are defined similarly but are computed based on $\mathbf{u}_{D,\mathrm{appr}}(\mathbf{x}, t)$ instead of $\mathbf{u}_D(\mathbf{x}, t)$.

Recall that, similarly as in Subsection 5.1, the repetitive nature of the applied heat load is exploited in the construction of $e_{\mathrm{appr}}(\mathbf{x})$ and $\mathbf{u}_{e,\mathrm{appr}}(\mathbf{x})$ based on the single-field responses $T_{\mathrm{pass}}(\mathbf{x}, t)$ and $\mathbf{u}_{\mathrm{pass}}(\mathbf{x}, t)$, but that such an approach is not possible in the computation of $e(\mathbf{x})$ and $\mathbf{u}_e(\mathbf{x})$ by the used standard FE method.

Table 9. The number of spatial and temporal grid points used to compute $e(\mathbf{x})$, $e_{\text{appr}}(\mathbf{x})$, $\mathbf{u}_e(\mathbf{x})$, and $\mathbf{u}_{e,\text{appr}}(\mathbf{x})$ for the whole wafer.

L_e [mm]	# spatial grid points			# temporal grid points	
	$e(\mathbf{x}), e_{\text{appr}}(\mathbf{x})$ $\mathbf{u}_e(\mathbf{x}), \mathbf{u}_{e,\text{appr}}(\mathbf{x})$	$T_{\text{pass}}(\mathbf{x},t)$ $\mathbf{u}_{\text{pass}}(\mathbf{x},t)$	$\mathbf{u}_D^{(BC)}(\mathbf{x},t)$	$e(\mathbf{x}), e_{\text{appr}}(\mathbf{x})$ $\mathbf{u}_e(\mathbf{x}), \mathbf{u}_{e,\text{appr}}(\mathbf{x})$	$T_{\text{pass}}(\mathbf{x},t)$ $\mathbf{u}_{\text{pass}}(\mathbf{x},t)$
2	17,665	2,132	793	2,193	216
1	70,681	8,343	3,146	4,385	431
1/2	282,697	33,005	12,291	8,769	861
1/4	1,130,913	131,289	48,581	17,537	1721

5.4.1. The first five fields

The overlay map is first computed for the same time interval as in the previous subsection, so for $t \in [0, t_1]$ with $t_1 = 0.628$ s. The overlay map is computed field-by-field, meaning that, for each field, $\mathbf{u}_D(\mathbf{x}, t)$ is computed only in the spatial grid points in the considered field and in the temporal grids points during which the current field is being scanned. It is straightforward to compute $e(\mathbf{x})$ and $\mathbf{u}_e(\mathbf{x})$ in (80a) and (80b) based on this data.

The spatial and temporal grids are essentially the same as in the previous subsection. The only difference is that the grid used to compute $\mathbf{u}_{D,\text{appr}}^{(BC)}(\mathbf{x}, t)$ changes with the currently considered field and now covers the area $(r, \theta) \in [98, 150]$mm $\times [\theta_i - 0.8, \theta_i + 0.8]$ rad, where θ_i denotes the θ-component of the center of the i-th field. The number of spatial and temporal grid points are thus still the same as in Table 2.

The obtained overlay map is shown in Figure 9. The maximum overlay, that is $\max_{\mathbf{x}} e(\mathbf{x})$, is 4.9 nm. Note that for all fields except the first one, $\mathbf{u}_{e,\text{appr}}(x, y)$ has a significant component in the negative x_1-direction due to thermal expansion in the previously scanned fields.

The MA overlay maps $e_{\text{appr}}(\mathbf{x})$ and MA deformation $\mathbf{u}_{e,\text{appr}}(\mathbf{x})$ obtained using the MoI will be compared to the overlay maps $e(\mathbf{x})$ and $\mathbf{u}_e(\mathbf{x})$ obtained by the used standard FE method. The times required to compute $e_{\text{appr}}(x, y)$ and $\mathbf{u}_{e,\text{appr}}(\mathbf{x})$ using the MoI and the times to compute $e(x, y)$ and $\mathbf{u}_e(\mathbf{x})$ by the used standard FE method are compared in Table 7. Note that the overlay map on the $L_e = 1/8$ mm grid is computed on a desktop with 32 GB RAM. Especially for smaller element sizes L_e, the construction using the MoI is significantly faster. Note that most of the computational time for the MoI is spent on the computation of the single-field response $\mathbf{u}_{\text{pass}}(\mathbf{x}, t)$ and that the times in Table 7 are significantly longer than the times for the construction of the snapshots given in Tables 3 and 4 because the computation of the overlay map requires the computation of the deformation at all considered time instances and not just at the final time instance.

The absolute and relative error in the overlay map $e_{\text{appr}}(\mathbf{x})$ (computed using the MoI) and in the overlay map $e(\mathbf{x})$ (computed by the used standard FE method) are compared in Table 8. The accuracy of both methods is similar on most of the considered grids. It seems that the accuracy of $e_{\text{appr}}(\mathbf{x})$ stops decreasing at the $L_e = 1/2$ mm grid. This was also observed for the accuracy of the displacement field $\mathbf{u}_{D,\text{appr}}(\mathbf{x}, t_1)$ in Table 6 and seems to indicate that the error due to the approximation of $\omega_D(r, \hat{\theta}, r')$ in (70a) by $\omega_{D,\text{appr}}(r, \hat{\theta}, r')$ starts to dominate. It is interesting to observe that the absolute error in $e_{\text{appr}}(\mathbf{x})$ is already below the typically required accuracy of 0.1 nm. The error in the MA deformation $\mathbf{u}_{e,\text{appr}}(\mathbf{x})$ and $\mathbf{u}_e(\mathbf{x})$ is of a similar magnitude as the error in the overlay $e(\mathbf{x})$ and $e_{\text{appr}}(\mathbf{x})$ reported in Table 8 and is therefore not reported here.

The maximal errors the FE solutions $e(\mathbf{x})$ and $\mathbf{u}_e(\mathbf{x})$ occur for all considered grids around the point $(x_1, x_2) = (-61, -132)$ mm, which is the left point closest to edge inside the five considered fields. The maximal error in the MoI solutions $e_{\text{appr}}(\mathbf{x})$ and $\mathbf{u}_e(\mathbf{x})$ occurs in the rightmost field; on the $L_e = 2$ mm and $L_e = 1$ mm grids around $(x_1, x_2) = (61, -132)$ and for the $L_e = 1/2$ mm and $L_e = 1/4$ mm grids around $(x_1, x_2) = (39, -132)$ mm. This observation and the accuracy of the FE solutions on the $L_e = 1/4$ mm grid indicate that the accuracy of the used reference solution does not significantly influence the errors in $e_{\text{appr}}(\mathbf{x})$ and $\mathbf{u}_{e,\text{appr}}(\mathbf{x})$, see Tables 8 and 6.
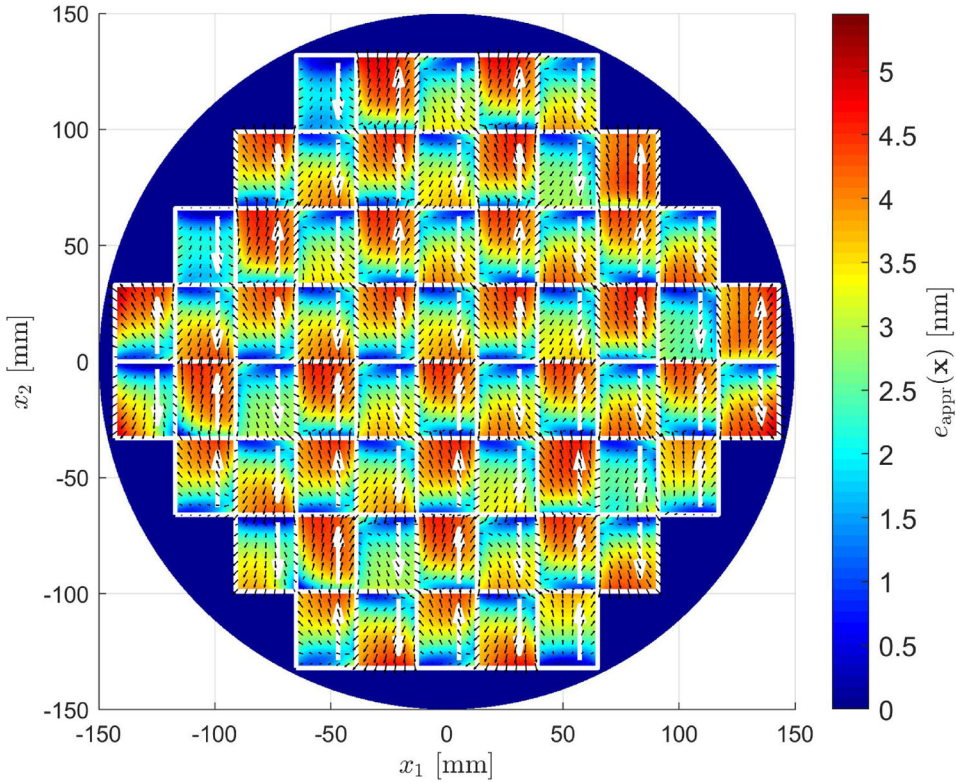
Figure 10. Overlay map constructed using the MoI on a uniform $L_e = 1/4$ mm grid. The color scale and the black arrows indicate $e_{\mathrm{appr}}(\mathbf{x})$ and $\mathbf{u}_{e,\mathrm{appr}}(\mathbf{x})$, respectively. The white rectangles with arrows indicate the considered fields with their scanning directions.

5.4.2. All fields on the wafer

The overlay map is now constructed for all fields on the wafer, meaning that the length of the considered time interval $I = [0, t_2]$ is increased to $t_2 = 8.768$ s. The spatial grid used for the FE solution is now based on a rectangular grid that covers the area $(x_1, x_2) \in [-150, 150] \times [-150, 150]$ mm^2 with a uniform grid spacing of L_e in both the x_1- and x_2-directions, but elements that (partially) fall outside D are discarded. The temporal grid for the FE solution covers the time interval $[0, t_2]$ with a uniform step size L_e/v_e, where $v_e = 0.5$ m/s. The spatial grid for the computation of $\mathbf{u}_{\mathrm{pass}}(\mathbf{x}, t)$ remains unchanged but the temporal grid now covers the interval $[0, t_{f2}]$ with $t_{f2} = 2.996$ s. The time step is L_e/v_e when $t \in [0, t_{f1}]$ with $t_{f1} = 0.148$ s (during which a heat load is applied) and $4L_e/v_e$ when $t \in (t_{f1}, t_{f2}]$ (during which no heat load is applied). The grid for the edge correction $\mathbf{u}_{D,\mathrm{appr}}^{(BC)}(\mathbf{x}, t)$ remains unchanged. The resulting number of spatial and temporal grid points are given in Table 9.

The overlay map computed using the MoI on the $L_e = 1/4$ mm grid is shown in Figure 10. The maximum of the MA overlay $e(\mathbf{x})$ is 5.5 nm, which shows that control is necessary to reduce the overlay to the subnanometer level required in modern wafer scanners.

The times required for the computation of $e(\mathbf{x})$ and $\mathbf{u}_e(\mathbf{x})$ using the MoI and by the used standard FE method are compared in Table 10. Even the 32 GB RAM of the used desktop PC was not sufficient to compute the FE solution on the $L_e = 1/4$ mm grid within a reasonable
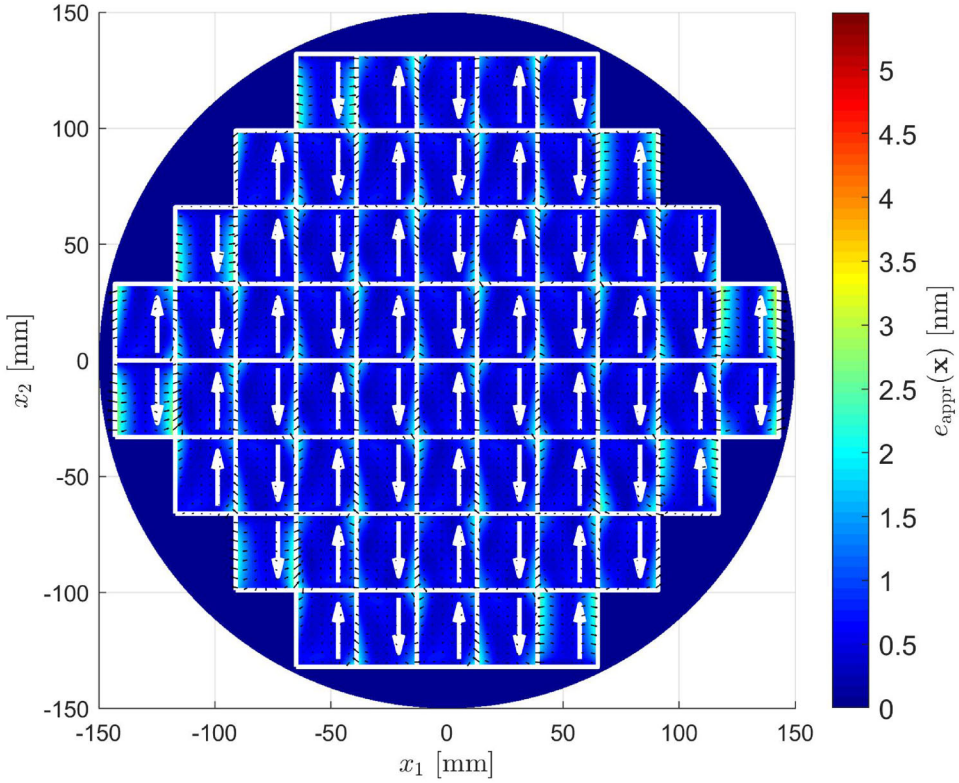
Figure 11. Overlay map obtained by the MoI when the rigid-body translations in the x_1- and x_2-directions of the wafer stage are used reduce the overlay error. The color scale and the black arrows indicate $e_{appr}(\mathbf{x})$ and $\mathbf{u}_{e,appr}(\mathbf{x})$, respectively. The white rectangles with arrows indicate the considered fields with their scanning directions.

Table 10. Computational times for the overlay map of the whole wafer using the MoI and by the used standard FE method.

L_e [mm]	$\mathbf{u}_{pass}$	MoI	FE
2	1.3 s	9.4 s	140.3 s
1	5.4 s	26.7 s	1187.5 s
1/2	56.4 s	256.7 s	10493.5 s
1/4	754.4 s	2577.5 s	–

amount of time. We were therefore not able to determine an accurate reference solution and the accuracy of the results of the simulation that considers all fields on the wafer could not be reported in the same way as for the simulation that considers only the first five fields. However, we expect that the accuracy of these results will be similar to the accuracy reported in Tables 5, 6, and 8 because the error introduced by the MoI will be the largest near the edge of the wafer.

Table 10 shows that making use of the repetitive nature of the heat load in the MoI significantly reduces computational time, especially on fine grids. Note that the time to compute $\mathbf{u}_{pass}(\mathbf{x},t)$ is now relatively small compared to the total time required to compute $e(\mathbf{x})$ and $\mathbf{u}_e(\mathbf{x})$. Most of the computational time is spent during the evaluation of the infinite domain solutions $T_{D,\infty}(\mathbf{x},t)$ and $\mathbf{u}_{D,\infty}(\mathbf{x},t)$ according to (19) and (22), which involves interpolation of the solutions $T_{pass}(\mathbf{x},t)$ and $\mathbf{u}_{pass}(\mathbf{x},t)$. It might be possible to reduce this time further with a smarter choice of spatial grids and/or a different interpolation method.

5.4.3. Wafer stage positioning

The imaging quality can be improved by adapting the position of the wafer stage that moves the wafer under the projection light. The overlay map in Figure 11 shows results of such an approach in which the two translations in x_1- and x_2-direction are used to reduce the overlay error. In particular, the overlay $e(\mathbf{x})$ and the MA deformation $\mathbf{u}_e(\mathbf{x})$ in this figure are obtained by replacing $\mathbf{u}_D(\mathbf{x}, t)$ in (80a) and (80b) by

$$\mathbf{u}_{D,c}(\mathbf{x}, t) = \mathbf{u}_D(\mathbf{x}, t) - \iint_{\Omega_{\text{slit}}(t)} \mathbf{u}_D(\mathbf{x}, t) \mathrm{d}\mathbf{x}, \tag{81}$$

where $\Omega_{\text{slit}}(t) \subset \mathbb{R}^2$ denotes the area of the slit (i.e. the area in which the heat load is applied) at time t. These rigid-body corrections reduce the maximal overlay error from 5.5 nm without corrections to less than 3.5 nm.

The computational times with corrections are very similar to the times without corrections given in Table 10. The proposed method thus provides an efficient way to test various correction strategies. This efficiency is important because these corrections should eventually be implemented in the wafer scanner, which means they have to be computed just before or during the exposure of the wafer.

6. Conclusions and recommendations

The results in this paper extend the classic MoI in two ways. Both extensions are based on the reformulation of the MoI on an arbitrary spatial domain $\Omega \subset \mathbb{R}^n$ in terms of a convolution kernel $\omega_\Omega(\mathbf{x}, \mathbf{x}')$ that should satisfy the conditions in Proposition 1. First, the kernel representation for the MoI enables the application of the MoI to heat-induced deformations. This extension is based on the displacement potential, which means that in most cases an additional elasticity problem needs to be solved to satisfy the mechanical BCs. Secondly, an analytic expression for the convolution kernel for the disk has been derived. Because the convolution with this kernel is expensive to compute, an approximation with lower computational cost has been derived as well. This enables the application of the MoI to a circular domains, which was not possible before.

These two extensions have been applied to a wafer heating problem in which the MoI is used to exploit the repetitive nature of the heat load. A reduction of more than a factor 10 in computation time could be achieved, see Table 10. Although the accuracy of the solutions constructed using the MoI on the disk is limited by the approximation of the convolution kernel, the discretization error in solutions computed by the used standard FE method is similar to the error in solutions obtained using the MoI on most of the considered grids. The total time to construct the overlay map with the MoI on a 2 mm grid is now 9.4 seconds. This is about the same time it takes to process one wafer. The proposed method can thus potentially be used for real-time prediction and correction.

The proposed extension of the MoI can be applied to a spatial domain Ω when a kernel ω_Ω that satisfies the conditions in Proposition 1 has been found. The existence of such a kernel has been demonstrated for several examples, but can in general not be guaranteed, see Remark 8. It is therefore an interesting topic for future research to investigate which spatial domains Ω admit a convolution kernel ω_Ω that satisfies the conditions in Proposition 1.

The proposed method requires the storage of the responses $T_{\text{pass}}(\mathbf{x}, t)$ and $\mathbf{d}_{\text{pass}}(\mathbf{x}, t)$ resulting from the scanning of a single field at all considered time instances, which can take up a significant amount of memory. On the $L_e = 1/4$ mm grid, this requires for example more than 1 GB of memory. The required amount of memory can potentially be reduced by semi-analytic techniques such as discussed in [11] or by model order reduction, see for example [29].

Although a closed-form analytic formula for the kernel on the disk has been derived, an approximation consisting of a single Dirac delta has been used in the numerical example in

Section 5. The error resulting from this approximation is acceptable in the considered wafer heating application, but other applications might require more accurate approximations. It would therefore be interesting to investigate how more accurate approximations can be obtained. As the convolution with these approximations should be easy to evaluate, it seems most natural to look for approximations consisting of multiple Dirac deltas.

Two additional difficulties in the simulation of wafer heating have not been considered in Section 5. First of all, it has been assumed that the heat load moves instantaneously to the next field after the scanning the previous field has been completed. In reality, this process will take some time that is not known exactly before the exposure of the wafer. Such uncertain timings can be incorporated easily in the proposed method by modifying the time shifts τ_i in (19) and (22) and can thus be incorporated after the solutions for the single field have been computed. Secondly, it should be noted that all fields in the heat load in Figure 1 fit fully on the wafer. However, to maximize the number of integrated circuits on each wafer, wafers often also contain fields that do not fit completely on the wafer. Such incomplete fields have not been considered. As each of these incomplete fields will typically have a different position w.r.t. the edge of the wafer, the exposure of each half field will typically require an additional (single-field) simulation.

Finally, it is interesting to note that the overlay clearly depends on the order in which the fields on the wafer are scanned. Designing an alternative ordering that leads to a better imaging quality (without significantly increasing the processing time) is an interesting topic for future research. The proposed method seems an ideal tool to evaluate the overlay resulting from various potential orderings quickly and accurately.

Appendix A. Proofs of proposition 1 and lemma 1

Proof of Proposition 1. It will be shown that substitution of (27d) in the LHS and RHS of (27b) and (27c) yields the same results when the conditions in (28) hold.

Substitution of (27d) in the LHS of (27b) yields

$$
\begin{aligned}
c\frac{\partial \tilde{T}_\Omega}{\partial t}(\mathbf{x},t) &= \iint_{\Omega^c}\omega_\Omega(\mathbf{x},\mathbf{x}')c\frac{\partial T_{\Omega,\infty}}{\partial t}(\mathbf{x}',t)\,\mathrm{d}\mathbf{x}'\\
&= \iint_{\Omega^c}\omega_\Omega(\mathbf{x},\mathbf{x}')\big(\kappa\nabla'^2 T_{\Omega,\infty}(\mathbf{x}',t)-h_0 T_{\Omega,\infty}(\mathbf{x}',t)\big)\,\mathrm{d}\mathbf{x}'\\
&= \kappa\iint_{\Omega^c}\omega_\Omega(\mathbf{x},\mathbf{x}')\nabla'^2 T_{\Omega,\infty}(\mathbf{x}',t)\mathrm{d}\mathbf{x}' - h_0\tilde{T}_\Omega(\mathbf{x},t),
\end{aligned}
\tag{A.1}
$$

where the second identity follows because $T_{\Omega,\infty}$ satisfies (1a) and the heat load $Q_{\Omega,\infty}$ is zero outside Ω according to (16). Inserting (27d) in the RHS of (27b) yields

$$
\kappa\nabla^2\tilde{T}_\Omega(x,y,t)-h_0\tilde{T}_\Omega(x,y,t)=\kappa\iint_{\Omega^c}\nabla^2\omega_\Omega(\mathbf{x},\mathbf{x}')T_{\Omega,\infty}(\mathbf{x}',t)\mathrm{d}\mathbf{x}' - h_0\tilde{T}_\Omega(\mathbf{x},t).
\tag{A.2}
$$

To see that the expressions on the RHS of (A.1) and (A.2) are equal, note that one of Green's identities, see for example [2], shows that

$$
\begin{aligned}
\iint_{\Omega^c}\omega_\Omega\nabla'^2 T_{\Omega,\infty}\mathrm{d}\mathbf{x}' &= \iint_{\Omega^c}\big(\nabla'^2\omega_\Omega\big)T_{\Omega,\infty}\,\mathrm{d}\mathbf{x}' + \int_{\partial\Omega}\big(\omega_\Omega\nabla' T_{\Omega,\infty}-T_{\Omega,\infty}\nabla'\omega_\Omega\big)\cdot\mathbf{n}\,\mathrm{d}\ell'\\
&= \iint_{\Omega^c}\big(\nabla'^2\omega_\Omega\big)T_{\Omega,\infty}\mathrm{d}\mathbf{x}' = \iint_{\Omega^c}\nabla^2\omega_\Omega T_{\Omega,\infty}\,\mathrm{d}\mathbf{x}',
\end{aligned}
\tag{A.3}
$$

where the dependence of ω_Ω on $(\mathbf{x},\mathbf{x}')$ and of $T_{\Omega,\infty}$ on $(\mathbf{x}',t)$ has been omitted, and $\mathbf{n}=\mathbf{n}(\mathbf{x}')$ denotes the outward pointing normal of Ω which is the inward pointing normal of Ω^c. The second identity in (A.3) follows because (28b) shows that the boundary terms vanish and the last identity in (A.3) follows from (28a). It thus follows that $\tilde{T}_\Omega$ in (27d) satisfies the PDE (27b).

For the BC (27c), note that the LHS of (27c) can be rewritten as

$$\nabla \tilde{T}_\Omega(\mathbf{x}, t) \cdot \mathbf{n}(\mathbf{x}) = \iint_{\Omega^c} T_{\Omega,\infty}(\mathbf{x}', t) \nabla \omega_\Omega(\mathbf{x}, \mathbf{x}') \cdot \mathbf{n}(\mathbf{x}) \, \mathrm{d}\mathbf{x}' = \iint_{\Omega^c} T_{\Omega,\infty}(\mathbf{x}', t) \nabla' \delta(\mathbf{x} - \mathbf{x}') \, \mathrm{d}\mathbf{x}' \cdot \mathbf{n}(\mathbf{x}). \tag{A.4}$$

For the RHS of (27c), note that

$$-\nabla T_{\Omega,\infty}(\mathbf{x}, t) \cdot \mathbf{n}(\mathbf{x}) = -\iint_{\Omega^c} \delta(\mathbf{x} - \mathbf{x}') \nabla' T_{\Omega,\infty}(\mathbf{x}', t) \, \mathrm{d}\mathbf{x}' \cdot \mathbf{n}(\mathbf{x}) = \iint_{\Omega^c} T_{\Omega,\infty}(\mathbf{x}', t) \nabla' \delta(\mathbf{x} - \mathbf{x}') \, \mathrm{d}\mathbf{x}' \cdot \mathbf{n}(\mathbf{x}), \tag{A.5}$$

where the last identity follows from the definition of the derivative of the Dirac delta in (29). The function $\tilde{T}_\Omega$ in (27d) thus also satisfies the BC (27c). □

Proof of Lemma 1. To see that $\tilde{\psi}_\Omega(\mathbf{x}, t)$ defined by (34b) indeed satisfies (35a), note that the definition (34b) shows that

$$\begin{aligned} (2\mu + \lambda)\nabla^2 \tilde{\psi}_\Omega &= (2\mu + \lambda)\iint_{\Omega^c} (\nabla^2 \omega_\Omega)\psi_{\Omega,\infty} \, \mathrm{d}\mathbf{x}' = (2\mu + \lambda)\iint_{\Omega^c} (\nabla'^2 \omega_\Omega)\psi_{\Omega,\infty} \, \mathrm{d}\mathbf{x}' \\ &= (2\mu + \lambda)\iint_{\Omega^c} \omega_\Omega(\nabla'^2 \psi_{\Omega,\infty}) \, \mathrm{d}\mathbf{x}' + (2\mu + \lambda)\int_{\partial\Omega} (\omega_\Omega \nabla' \psi_{\Omega,\infty} - \psi_{\Omega,\infty} \nabla' \omega_\Omega) \cdot \mathbf{n} \, \mathrm{d}\ell' \\ &= \iint_{\Omega^c} \omega_\Omega(\tilde{k}_0 \psi_{\Omega,\infty} + (2\mu + n\lambda)\alpha T_{\Omega,\infty}) \, \mathrm{d}\mathbf{x}' = \tilde{k}_0 \tilde{\psi}_\Omega + (2\mu + n\lambda)\alpha \tilde{T}_\Omega, \end{aligned} \tag{A.6}$$

where the second identity follows from the first condition for the kernel $\omega_\Omega(\mathbf{x}, \mathbf{x}')$ in (28a), the third identity follows from one of Green's identities, the fourth identity because the boundary terms vanish due to second condition for $\omega_\Omega(\mathbf{x}, \mathbf{x}')$ (28b) and because $\psi_{\Omega,\infty}(\mathbf{x}, t)$ is defined as the solution of (10), and the last identity from the definitions of $\tilde{\psi}_\Omega(\mathbf{x}, t)$ and $\tilde{T}_\Omega(\mathbf{x}, t)$ in (34b) and (27d). Note that the dependence of $\tilde{\psi}_\Omega$ and $\tilde{T}_\Omega$ on $(\mathbf{x}, t)$, the dependence of $\psi_{\Omega,\infty}$ and $T_{\Omega,\infty}$ on $(\mathbf{x}', t)$, and the dependence of ω_Ω on $(\mathbf{x}, \mathbf{x}')$ has been dropped in (A.6). It thus follows that $\tilde{\psi}_\Omega(\mathbf{x}, t)$ in (34b) indeed satisfies (35a).

For the BC (35b), note that for $\mathbf{x} \in \partial\Omega$

$$\begin{aligned} \nabla\tilde{\psi}_\Omega(\mathbf{x}, t) \cdot \mathbf{n}(\mathbf{x}) &= \iint_{\Omega^c} (\nabla\omega_\Omega(\mathbf{x}, \mathbf{x}') \cdot \mathbf{n}(\mathbf{x}))\psi_{\Omega,\infty}(\mathbf{x}', t) \, \mathrm{d}\mathbf{x}' = \iint_{\Omega^c} (\nabla'\delta(\mathbf{x} - \mathbf{x}') \cdot \mathbf{n}(\mathbf{x}))\psi_{\Omega,\infty}(\mathbf{x}', t) \, \mathrm{d}\mathbf{x}' \\ &= \iint_{\Omega^c} (\nabla'\delta(\mathbf{x} - \mathbf{x}'))\psi_{\Omega,\infty}(\mathbf{x}', t) \, \mathrm{d}\mathbf{x}' \cdot \mathbf{n}(\mathbf{x}) = -\iint_{\Omega^c} \nabla'\psi_{\Omega,\infty}(\mathbf{x}', t)\delta(\mathbf{x} - \mathbf{x}') \, \mathrm{d}\mathbf{x}' \cdot \mathbf{n}(\mathbf{x}) = -\nabla\psi_{\Omega,\infty}(\mathbf{x}, t) \cdot \mathbf{n}(\mathbf{x}), \end{aligned} \tag{A.7}$$

where the first identity follows from the expression for $\tilde{\psi}_\Omega(\mathbf{x}, t)$ in (34b), the second identity from the third condition for $\omega_\Omega(\mathbf{x}, \mathbf{x}')$ in (28c), the third identity by pulling the normal $\mathbf{n}(\mathbf{x})$ out of the integral, the fourth identity from the definition of the derivative of a Dirac delta in (29), and the fifth identity from the definition of the Dirac delta. The BC (35b) is thus indeed satisfied by $\tilde{\psi}_\Omega(\mathbf{x}, t)$ defined in (34b). □

Appendix B. Boundary conditions and the weak form

In this appendix, it is demonstrated that the BCs in (40) and (66) for the kernels $\omega_{HP}(x_1, \hat{x}_2, x_1')$ on the half plane HP and $\omega_D(r, \hat{\theta}, r')$ on the disk D are (in the weak sense) equivalent to the BCs (41) and (68), respectively.

B.1. The half plane

The weak form of (40) is found by multiplying (40a) by a test function $f = f(x_1, \hat{x}, x_1')$ and integrating over $(x_1, \hat{x}, x_1') \in HP \times [x_e, x_e + \varepsilon]$. This leads to

$$\begin{aligned} \iint_{HP} \left(f\frac{\partial \omega_{HP}}{\partial x_1'} - \frac{\partial f}{\partial x_1'}\omega_{HP} \right) \mathrm{d}x_1 \mathrm{d}\hat{x} \Big|_{x_1' = x_e}^{x_e+\varepsilon} &+ \int_{x_e}^{x_e+\varepsilon} \iint_{HP} \frac{\partial^2 f}{\partial x_1'^2}\omega_{HP} \, \mathrm{d}x_1 \, \mathrm{d}\hat{x} \, \mathrm{d}x_1' \\ &= -\int_{\mathbb{R}} \frac{\partial f}{\partial x_1'} \Big|_{(x_1, x_1')=(x_e, x_e)} \delta(\hat{x}) \, \mathrm{d}\hat{x} - \int_{x_e}^{x_e+\varepsilon} \iint_{HP} \frac{\partial f}{\partial x_1}\frac{\partial \omega_{HP}}{\partial x_1} \, \mathrm{d}x_1 \mathrm{d}\hat{x} \, \mathrm{d}x_1'. \end{aligned} \tag{B.1}$$

The LHS of (B.1) has been obtained from $f \frac{\partial^2 \omega_{HP}}{\partial x_1'^2}$ using integration by parts over x_1' twice. The RHS of (B.1) has been obtained by rewriting $f \frac{\partial^2 \omega_{HP}}{\partial x_1^2}$ using integration by parts over x_1, the BC (40c), and the definition of derivative of the Dirac delta in (29).

When taking the limit $\varepsilon \to 0$, the integrals over x_1' converge to zero. Note that (40b) shows that the boundary terms on the LHS of (B.1) at $x = x_1'$ vanish as well. Because the test function $f(x_1, \hat{x}, x_1')$ is smooth, it thus follows that

$$\lim_{\varepsilon \to 0} -\frac{\partial f}{\partial x_1'}(x_1, \hat{x}, x_e)\omega_{HP}(x_1, \hat{x}, x_e + \varepsilon) = -\frac{\partial f}{\partial x_1'}(x_1, \hat{x}, x_e)\delta(x - x_e)\delta(\hat{x}), \tag{B.2a}$$

$$\lim_{\varepsilon \to 0} f(x_1, \hat{x}, x_e)\frac{\partial \omega_{HP}}{\partial x_1'}(x_1, \hat{x}, x_e + \varepsilon) = 0, \tag{B.2b}$$

Conditions (41a) and (41b) now follow because (B.2) must hold for any (smooth) test function $f(x_1, \hat{x}, x_1')$. The last condition (41c) simply follows by noting that (40c) reduces to (41c) for $x_1' > x_e$.

B.2. The disk

To remove the derivative of the Dirac delta in (66c), the weak form of (66) is derived by multiplying (66a) by $f(r, \hat{\theta}, r')r'r$, where $f(r, \hat{\theta}, r')$ is a test function, and integrating over $(r, \hat{\theta}, r') \in (0, R) \times (0, 2\pi) \times (R, R + \varepsilon)$. This yields

$$\int_{-\pi}^{\pi} \int_0^R \left[f\frac{\partial \omega_D}{\partial r'} - \frac{\partial f}{\partial r'}\omega_D \right] r'r \, dr \, d\hat{\theta} \Big|_{r'=R}^{R+\varepsilon} + \int_R^{R+\varepsilon} \int_{-\pi}^{\pi} \int_0^R \left[\frac{\partial}{\partial r'}\left(r'\frac{\partial f}{\partial r'} \right) + \frac{1}{r'}\frac{\partial^2 f}{\partial \hat{\theta}^2} \right] \omega_D r \, dr \, d\hat{\theta} \, dr'$$

$$= -\int_{-\pi}^{\pi} \frac{\partial f}{\partial r'}\Big|_{(r, r')=(R, R)} R\delta(\hat{\theta}) \, d\hat{\theta} - \int_R^{R+\varepsilon} \int_{-\pi}^{\pi} \int_0^R \left(\frac{\partial f}{\partial r}\frac{\partial \omega_D}{\partial r} + \frac{1}{r^2}\frac{\partial f}{\partial \hat{\theta}}\frac{\partial \omega_D}{\partial \hat{\theta}} \right) r'r \, dr \, d\hat{\theta} \, dr'. \tag{B.3}$$

The LHS of (B.3) has been obtained by integration by parts over r' and $\hat{\theta}$ (the boundary terms at $\hat{\theta} = -\pi$ and $\hat{\theta} = \pi$ vanish because of the periodicity in the $\hat{\theta}$-direction). The RHS of (B.3) has been obtained using integration by parts over r and $\hat{\theta}$, the BC (66c), and the definition of the derivative of the Dirac delta. Similarly as before, the integrals over r' vanish when taking the limit $\varepsilon \to 0$ and the boundary terms on the LHS at $r' = R$ vanish because of (66b). It thus follows that

$$\lim_{\varepsilon \to 0} -\frac{\partial f}{\partial r'}(r, \hat{\theta}, R)\omega_D(r, \hat{\theta}, R + \varepsilon)Rr = \frac{\partial f}{-\partial r'}(r, \hat{\theta}, R)R\delta(R - r)\delta(\hat{\theta}), \tag{B.4a}$$

$$\lim_{\varepsilon \to 0^-} f(r, \hat{\theta}, R)\frac{\partial \omega_D}{\partial r'}(r, \hat{\theta}, R + \varepsilon)Rr = 0. \tag{B.4b}$$

As (B.4) must hold for any test function $f(r, \hat{\theta}, r')$, (68a) and (68b) follow. The BC (68c) follows by noting that (66c) reduces to (68c) for $r' > R$.

Appendix C. The kernel for the disk

An explicit expression for $\omega_{D,\gamma}(r, \hat{\theta}, r')$ satisfying (66a) and (68) with the Dirac in (68a) replaced by $\delta_\gamma(r - R, \hat{\theta})$ in (69) is obtained by noting that, at every 'time instant' $r', \omega_D(r, \hat{\theta}, r')$ can be expressed in terms of the eigenfunctions of the Laplacian on the disk $(r, \hat{\theta}) \in [0, R) \times [-\pi, \pi]$. The eigenfunctions of the Laplacian that are in agreement with the BC (68c) are, see for example [30]

$$w_{n,m}(r, \hat{\theta}) = J_n\left(\beta_{n,m}\frac{r}{R} \right)\cos(n\hat{\theta}), \ n \geq 0, m \geq 1, \tag{C.1a}$$

$$\tilde{w}_{n,m}(r, \hat{\theta}) = J_n\left(\beta_{n,m}\frac{r}{R} \right)\sin(n\hat{\theta}), \ n \geq 1, m \geq 1, \tag{C.1b}$$

where J_n is the Bessel function of the first kind of order n and $\beta_{n,m}$ is the m-th zero of $\partial J_n/\partial r(r) = 0$. Note that $\beta_{0,1} = 0$ and that $J_0(0) = 1$, so that $w_{0,1}(r, \hat{\theta}) \equiv 1$. The kernel $\omega_D(r, \hat{\theta}, r')$ can thus be written as

$$\omega_D(r, \hat{\theta}, r') = \sum_{n=0}^{\infty}\sum_{m=1}^{\infty} a_{n,m}(r')w_{n,m}(r, \hat{\theta}) + \sum_{n=1}^{\infty}\sum_{m=1}^{\infty} \tilde{a}_{n,m}(r')\tilde{w}_{n,m}(r, \hat{\theta}), \tag{C.2}$$

where the coefficients $a_{n,m}(r')$, and $\tilde{a}_{n,m}(r')$ still need to be determined.

A set of ODEs for the coefficients $a_{n,m}(r')$ and $\tilde{a}_{n,m}(r')$ can be obtained through a Galerkin discretization of (66a). Using that the eigenvalue of the Laplacian associated to $w_{n,m}(r, \hat{\theta})$ and $w_{n,m}(r, \hat{\theta})$ is $-\beta_{n,m}^2/R^2$ and that the eigenfunctions are mutually orthogonal w.r.t. the natural inner product

$$\langle f, g \rangle = \int_0^R \int_{-\pi}^{\pi} f(r, \hat{\theta}) g(r, \hat{\theta}) r \, d\hat{\theta} \, dr, \tag{C.3}$$

it follows that inserting (C.2) into (66a) and taking the inner product with the shape functions $w_{n,m}(r, \hat{\theta})$ yields

$$\frac{1}{r'} \frac{\partial}{\partial r'} \left(r' \frac{\partial a_{n,m}}{\partial r'} (r') \right) - \frac{n^2}{r'^2} a_{n,m}(r') = \frac{-\beta_{n,m}^2}{R^2} a_{n,m}(r'), \tag{C.4a}$$

where the factor $\langle w_{n,m}, w_{n,m} \rangle$ has been omitted. Similarly, inserting (C.2) into (66a) and taking the inner product with the shape functions $\tilde{w}_{n,m}(r, \hat{\theta})$ yields

$$\frac{1}{r'} \frac{\partial}{\partial r'} \left(r' \frac{\partial \tilde{a}_{n,m}}{\partial r'} (r') \right) - \frac{n^2}{r'^2} \tilde{a}_{n,m}(r') = \frac{-\beta_{n,m}^2}{R^2} \tilde{a}_{n,m}(r'), \tag{C.4b}$$

where the factor $\langle \tilde{w}_{n,m}, \tilde{w}_{n,m} \rangle$ has been omitted. Recall that $\beta_{0,1} = 0$, so that the solution of (C.5b) for $(n, m) = (0, 1)$ is of the form

$$a_{0,1}(r') = A_{0,1} + B_{0,1} \log (r'/R), \tag{C.5a}$$

where $A_{0,1}$ and $B_{0,1}$ are constants. For all other values of n and m, the solution of (C.4a) is of the form

$$a_{n,m}(r') = A_{n,m} J_n(\beta_{n,m} r'/R) + B_{n,m} Y_n(\beta_{n,m} r'/R), \tag{C.5b}$$

where $Y_n(r)$ is the Bessel function of the second kind of order n and $A_{n,m}$ and $B_{n,m}$ are constants. Similarly, the solutions of (C.4b) take the form

$$\tilde{a}_{n,m}(r') = \tilde{A}_{n,m} J_n(\beta_{n,m} r'/R) + \tilde{B}_{n,m} Y_n(\beta_{n,m} r'/R), \tag{C.5c}$$

where $\tilde{A}_{n,m}$ and $\tilde{B}_{n,m}$ are constants.

The constants $A_{n,m}, B_{n,m}, \tilde{A}_{n,m}$, and $\tilde{B}_{n,m}$ are determined based on the initial conditions (68a) and (68b). Since the eigenfunctions $w_{n,m}(r, \hat{\theta})$ and $\tilde{w}_{n,m}(r, \hat{\theta})$ are linearly independent, (68b) implies that

$$\frac{\partial a_{0,1}}{\partial r'} (R) = 0, \quad \frac{\partial a_{n,m}}{\partial r'} (R) = 0, \quad \frac{\partial \tilde{a}_{n,m}}{\partial r'} (R) = 0. \tag{C.6}$$

Inserting the expressions for $a_{n,m}(r')$ and $\tilde{a}_{n,m}(r')$ in (C.5) into (C.6) and using that $\partial J_n / \partial r(\beta_{n,m}) = 0$, it follows that $B_{n,m} = 0$ and $\tilde{B}_{n,m} = 0$.

The constants $A_{n,m}$ and $\tilde{A}_{n,m}$ follow by inserting (C.2) into (68a) and projecting on $w_{n,m}(r, \hat{\theta})$ and $\tilde{w}_{n,m}(r, \hat{\theta})$. This yields

$$a_{n,m}(R) \langle w_{n,m}, w_{n,m} \rangle = \langle \omega_D(\cdot, \cdot, R), w_{n,m} \rangle = \langle \delta_\gamma(r - R, \hat{\theta}), w_{n,m} \rangle, \tag{C.7a}$$

$$\tilde{a}_{n,m}(R) \langle \tilde{w}_{n,m}, \tilde{w}_{n,m} \rangle = \langle \omega_D(\cdot, \cdot, R), \tilde{w}_{n,m} \rangle = \langle \delta_\gamma(r - R, \hat{\theta}), \tilde{w}_{n,m} \rangle. \tag{C.7b}$$

Note that $\tilde{a}_{n,m}(R) = 0$ because δ_γ is symmetric and $\tilde{w}_{n,m}$ is anti symmetric in $\hat{\theta} = 0$. Because $\tilde{B}_{n,m} = 0$, (C.5c) now shows that $\tilde{A}_{n,m} = 0$ and thus that $\tilde{a}_{n,m}(r') \equiv 0$. Inserting (C.1) and (C.5) with $B_{n,m} = 0$ into (C.2) now shows that $\omega_{D,\gamma}(r, \hat{\theta}, r')$ is of the form (70a).

The coefficients $A_{n,m}$ follow after inserting (C.5a) and (C.5b) into (C.7a) as

$$A_{n,m} = \frac{\langle \delta_\gamma(r - R, \hat{\theta}), w_{n,m} \rangle}{J_n(\beta_{n,m}) \langle w_{n,m}, w_{n,m} \rangle}. \tag{C.8}$$

The denominator in the expression for $A_{n,m}$ in (C.8) can be made more explicit by noting that

$$\langle w_{0,1}, w_{0,1} \rangle = \pi R^2, \tag{C.9a}$$

and for all other values of n and m, see for example [30],

$$\langle w_{n,m}, w_{n,m} \rangle = \frac{\epsilon_n}{2} \pi R^2 J_n^2(\beta_{n,m}) \left[1 - \frac{n^2}{\beta_{n,m}^2} \right], \tag{C.9b}$$

where $\epsilon_n = 2$ when $n = 0$ and $\epsilon_n = 1$ for $n \neq 0$.

The coefficients $A_{n,m}$ in (70b) for $\gamma = 0$ now follow from (C.8) and (C.9) by noting that

$$\langle \delta_0(r - R, \hat{\theta}), w_{n,m} \rangle = w_{n,m}(R, 0) = J_n(\beta_{n,m}), \tag{C.10}$$

where it was used that $\delta_\gamma(r - R, \hat{\theta})$ approaches a Dirac at $(r, \hat{\theta}) = (R, 0)$ for $\gamma \to 0$ and that $w_{n,m}(r, \hat{\theta})$ is given by (C.1a).

For $\gamma > 0$, the numerator in (C.8) can be rewritten using the expressions for $\delta_\gamma(r - R, \hat{\theta})$ in (69) and $w_{n,m}(r, \hat{\theta})$ in (C.1a) as

$$\langle \delta_\gamma(r - R, \hat{\theta}), w_{0,1} \rangle = 1 - \frac{\gamma}{2}\left(1 - \frac{4}{\pi^2}\right), \tag{C.11a}$$

for $n = 0$ and $m = 1$ and as

$$\langle \delta_\gamma(r - R, \hat{\theta}), w_{n,m} \rangle = C_{n,m} D_n, \tag{C.11b}$$

for all other values of n and m. Here, $C_{n,m}$ and D_n are

$$C_{n,m} = \frac{1}{\gamma R^2} \int_{(1-\gamma)R}^{R} J_n\left(\frac{\beta_{n,m} r}{R}\right)\left(1 + \cos\left(\frac{\pi(r - R)}{\gamma R}\right)\right) r \, dr, \tag{C.11c}$$

$$D_n = \frac{1}{2\gamma} \int_{-\gamma}^{\gamma} \cos(n\hat{\theta})\left(1 + \cos\left(\frac{\pi\hat{\theta}}{\gamma}\right)\right) d\hat{\theta} = \frac{\sin(n\gamma)}{n\gamma\left(1 - \frac{n^2\gamma^2}{\pi^2}\right)}. \tag{C.11d}$$

The integral in (C.11c) cannot be simplified further and is approximated numerically by a trapezoid quadrature rule.

Funding

ORCID

Daniel W. M. Veldman http://orcid.org/0000-0002-0767-2710
Rob H. B. Fey http://orcid.org/0000-0002-7778-5913
Hans Zwart http://orcid.org/0000-0003-3451-7967
Henk Nijmeijer http://orcid.org/0000-0001-5883-6191

References

[1] H. S. Carslaw and J. C. Jaeger, *Conduction of Heat in Solids*, 2nd ed. Oxford, UK: Oxford University Press, 1959.
[2] L. C. Evans, "Partial differential equations," 2010. 2nd ed. Providence, RI: Graduate Studies in Mathematics, volume 19, American Mathematical Society. DOI: 10.1090/gsm/019.
[3] D. Rosenthal, "The theory of moving sources of heat and its application of metal treatments," *Trans. ASME*, vol. 68, pp. 849–866, 1946.
[4] V. D. Fachinotti, A. A. Anca and A. Cardona, "Analytical solutions of the thermal field induced by moving double-ellipsoidal and double-elliptical heat sources in a semi-infinite body," *Int. J. Numer. Meth. Biomed. Engng.*, vol. 27, no. 4, pp. 595–607, 2011. DOI: 10.1002/cnm.1324.
[5] T. F. Flint, J. A. Francis, M. C. Smith and A. N. Vasileiou, "Semi-analytical solutions for the transient temperature fields induced by a moving heat source in an orthogonal domain," *Int. J. Thermal Sci.*, vol. 123, pp. 140–150, 2018. DOI: 10.1016/j.ijthermalsci.2017.09.012.
[6] C. J. Dias, "A method of recursive images to solve transient heat diffusion in multilayer materials," *Int. J. Heat Mass Transfer*, vol. 85, pp. 1075–1083, 2015. doi: 10.1016/j.ijheatmasstransfer.2015.01.138.
[7] C. J. Dias, "Transient heat diffusion in multilayered materials with thermal contact resistance," *Int. J. Heat Mass Transfer*, vol. 97, pp. 1001–1009, 2016. doi: 10.1016/j.ijheatmasstransfer.2016.02.079.
[8] G. H. Bryan, "An application of the method of images to the conduction of heat," *Proc. London Math. Soc.*, vol. s1-22, no. 1, pp. 424–430, 1890. DOI: 10.1112/plms/s1-22.1.424.
[9] J. Boersma, "Note on green's function for a semicircular plate," *Int. J. Solids Struct.*, vol. 17, no. 5, pp. 541–542, 1981. DOI: 10.1016/0020-7683(81)90060-3.
[10] P. A. Martin, "Scattering by defects in an exponentially graded layer and misuse of the method of images," *Int. J. Solids Struct.*, vol. 48, no. 14-15, pp. 2164–2166, 2011. doi: 10.1016/j.ijsolstr.2011.03.020.

[11] D. W. M. Veldman, R. H. B. Fey, H. Zwart, M. M. J. van de Wal, J. D. B. J. van den Boom and H. Nijmeijer, "Semi-analytic approximation of the temperature field resulting from moving heat loads," *Int. J. Heat Mass Transfer*, vol. 122, pp. 128–137, 2018. doi: 10.1016/j.ijheatmasstransfer.2018.01.085.

[12] R. Komanduri and Z. Hou, "Thermal analysis of the laser surface transformation hardening process," *Int. J. Heat Mass Transfer*, vol. 44, no. 15, pp. 2845–2862, 2001. DOI: 10.1016/S0017-9310(00)00316-1.

[13] J. D. Majumdar and I. Manna, "Laser material processing," *Int. Mater. Rev.*, vol. 56, no. 5-6, pp. 341–388, 2011. DOI: 10.1179/1743280411Y.0000000003.

[14] S. Oh and H. Ki, "Prediction of hardness and deformation using a 3-d thermal analysis in laser hardening of aisi h13 tool steel," *Appl. Thermal Eng.*, vol. 121, pp. 951–962, 2017. doi: 10.1016/j.applthermaleng.2017.04.156.

[15] W. E. Frazier, "Metal additive manufacturing: A review," *J. Mater. Eng. Perform.*, vol. 23, no. 6, pp. 1917–1928, 2014. DOI: 10.1007/s11665-014-0958-z.

[16] W. E. King, et al., "Laser powder bed fusion additive manufacturing of metals; physics, computational, and materials challenges," *Appl. Phys. Rev.*, vol. 2, no. 4, pp. 041304, 2015. DOI: 10.1063/1.4937809.

[17] E. J. Schwalbach, S. P. Donegan, M. G. Chapman, K. J. Chaput and M. A. Groeber, "A discrete source model of powder bed fusion additive manufacturing thermal history," *Additive Manufact.*, vol. 25, pp. 485–498, 2019. doi: 10.1016/j.addma.2018.12.004.

[18] L. Subramany, et al., "Analysis of wafer heating in 14nm DUV layers," Proceedings of the 2016 SPIE Conference on Metrology, Inspection, and Process Control for Microlithography XXX, Vol. 9778, International Society for Optics and Photonics, 2016. in: Pp. 275 – 281. DOI: 10.1117/12.2218724.

[19] D. van den Hurk, S. Weiland and K. van Berkel, "Modeling and localized feedforward control of thermal deformations induced by a moving heat load," Proceedings of the 2018 International Symposium on Control Systems of the Society of Instrument and Control Engineers (SICE-ISCS), 2018. in: Pp. 171–178. DOI: 10.23919/SICEISCS.2018.8330172.

[20] W. Nowacki, *Thermoelasticity*, 2nd ed. Warsaw, Poland: Pergamon, 1986. DOI: 10.1016/B978-0-08-024767-0.50007-1.

[21] A. D. Kovalenko, *Thermoelasticity: Basic Theory and Applications*. Groningen, the Netherlands: Wolters-Noordhoff, 1969.

[22] R. Hetnarski and M. Eslami, *Thermal Stresses: Advanced Theory and Applications, Solid Mechanics and Its Applications, Volume 158*, Dordrecht, the Netherlands: Springer, 2009. DOI: 10.1007/978-1-4020-9247-3.

[23] K. Feng and Z.-C. Shi, *Mathematical Theory of Elastic Structures*. Berlin, Germany: Springer, 1996. DOI: 10.1007/978-3-662-03286-2.

[24] F. John, "The ultrahyperbolic differential equation with four independent variables," *Duke Math. J.*, vol. 4, no. 2, pp. 300–322, 1938. DOI: 10.1215/S0012-7094-38-00423-5.

[25] A. Kurusa, "A characterization of the radon transform's range by a system of pdes," *J. Math. Anal. Applicat.*, vol. 161, no. 1, pp. 218–226, 1991. DOI: 10.1016/0022-247X(91)90371-6.

[26] G. Grubb, *Distributions and Operators*, Springer, New York, NY, 2009. DOI: 10.1007/978-0-387-84895-2_3.

[27] D. W. M. Veldman, R. H. B. Fey, H. Zwart, M. M. J. v. d. Wal, J. D. B. J. v. d. Boom and H. Nijmeijer, "Optimal thermal actuation for mitigation of heat-induced wafer deformation," *IEEE Trans. Contr. Syst. Technol.*, vol. 29, no. 2, pp. 514–529, 2021. DOI: 10.1109/TCST.2019.2948592.

[28] J. Crank and P. Nicolson, "A practical method for numerical evaluation of solutions of partial differential equations of the heat-conduction type," *Math. Proc. Camb. Phil. Soc.*, vol. 43, no. 1, pp. 50–67, 1947. DOI: 10.1017/S0305004100023197.

[29] A. C. Antoulas, Approximation of large-scale dynamical systems, advances in design and control, volume 6, SIAM, 2005. DOI: 10.1137/1.9780898718713.

[30] A. Gray and G. Mathews, *A Treatise on Bessel Functions and Their Applications to Physics*, 2nd Edition. Londen, UK: McMillan, 1952.